



ARL-TR-7285 • MAY 2015



US Army Research Laboratory

Coherent Optical Control of Electronic Excitations in Wide-Band-Gap Semiconductor Structures

by Sergey Rudin, Gregory Garrett, and Vladimir Malinovsky

Approved for public release; distribution is unlimited.

NOTICES

Disclaimers

The findings in this report are not to be construed as an official Department of the Army position unless so designated by other authorized documents.

Citation of manufacturer's or trade names does not constitute an official endorsement or approval of the use thereof.

Destroy this report when it is no longer needed. Do not return it to the originator.



Coherent Optical Control of Electronic Excitations in Wide-Band-Gap Semiconductor Structures

Sergey Rudin and Gregory Garrett
Sensors and Electron Devices Directorate, ARL

Vladimir Malinovsky
Oak Ridge Associated Universities
Oak Ridge, TN

REPORT DOCUMENTATION PAGE				Form Approved OMB No. 0704-0188	
<p>Public reporting burden for this collection of information is estimated to average 1 hour per response, including the time for reviewing instructions, searching existing data sources, gathering and maintaining the data needed, and completing and reviewing the collection information. Send comments regarding this burden estimate or any other aspect of this collection of information, including suggestions for reducing the burden, to Department of Defense, Washington Headquarters Services, Directorate for Information Operations and Reports (0704-0188), 1215 Jefferson Davis Highway, Suite 1204, Arlington, VA 22202-4302. Respondents should be aware that notwithstanding any other provision of law, no person shall be subject to any penalty for failing to comply with a collection of information if it does not display a currently valid OMB control number.</p> <p>PLEASE DO NOT RETURN YOUR FORM TO THE ABOVE ADDRESS.</p>					
1. REPORT DATE (DD-MM-YYYY) May 2015		2. REPORT TYPE DRI		3. DATES COVERED (From - To) October 2011–September 2014	
4. TITLE AND SUBTITLE Coherent Optical Control of Electronic Excitations in Wide-Band-Gap Semiconductor Structures				5a. CONTRACT NUMBER	
				5b. GRANT NUMBER	
				5c. PROGRAM ELEMENT NUMBER	
6. AUTHOR(S) Sergey Rudin, Gregory Garrett, and Vladimir Malinovsky				5d. PROJECT NUMBER	
				5e. TASK NUMBER	
				5f. WORK UNIT NUMBER	
7. PERFORMING ORGANIZATION NAME(S) AND ADDRESS(ES) US Army Research Laboratory ATTN: RDRL-SEE-I Aberdeen Proving Ground, MD 21005-5066				8. PERFORMING ORGANIZATION REPORT NUMBER ARL-TR-7285	
9. SPONSORING/MONITORING AGENCY NAME(S) AND ADDRESS(ES)				10. SPONSOR/MONITOR'S ACRONYM(S)	
				11. SPONSOR/MONITOR'S REPORT NUMBER(S)	
12. DISTRIBUTION/AVAILABILITY STATEMENT Approved for public release; distribution is unlimited.					
13. SUPPLEMENTARY NOTES					
14. ABSTRACT The main objective of this research is to study coherent quantum effects, such as Rabi oscillations in optical spectra of wide-band-gap materials, and to determine the feasibility of fast optical control of quantum states in gallium nitride and zinc oxide heterostructures. Because of much stronger exciton-photon interaction in these materials as compared to gallium arsenide, it is possible to realize the strong coupling regime at room temperature. We perform an experimental and theoretical study on the dephasing processes in available nitride and zinc oxide materials. This is a necessary work toward coherent optical control of quantum states at higher temperatures, with ultimately room-temperature coherent control. We also propose a scheme to perform arbitrary unitary operations on a single electron-spin qubit in a quantum dot. The design is solely based on the geometrical phase that the qubit state acquires after a cyclic evolution in the parameter space.					
15. SUBJECT TERMS wide-band-gap semiconductors, coherent control, dephasing processes, quantum gates					
16. SECURITY CLASSIFICATION OF:			17. LIMITATION OF ABSTRACT UU	18. NUMBER OF PAGES 68	19a. NAME OF RESPONSIBLE PERSON Sergey Rudin
a. REPORT Unclassified	b. ABSTRACT Unclassified	c. THIS PAGE Unclassified			19b. TELEPHONE NUMBER (Include area code) 301-394-0206

Contents

List of Figures	v
List of Tables	viii
Acknowledgments	ix
1. Objectives	1
1.1 Approach to Achieving the Objectives	1
1.2 Progress Made toward Achieving the Director's Research Initiative (DRI) Research Objectives	1
2. Temperature Effects in the Kinetics of Photoexcited Carriers in Wide-Band-Gap Semiconductors	2
2.1 Theoretical Model	3
2.2 Numerical Procedure	10
2.3 Experiment	11
2.4 Results and Discussion for the Gallium Nitride (GaN) Case	12
2.5 Summary for Gallium Nitride (GaN) Experiments and Modeling	23
2.6 Results and Discussion for the Zinc Oxide (ZnO) Case	23
3. Geometric Single-Qubit Quantum Gates for an Electron Spin in a Quantum Dot	27
3.1 Introduction	27
3.2 General Equations of Motion	28
3.3 Nonimpulsive Case	32
3.4 Adiabatic Solution	33
3.5 Bloch Vector Representation	37
3.6 Evolution Operator of the Bloch Vector	39
3.7 Ultrafast Qubit Rotations Using Geometrical Phase	39
3.8 Rotation in the Bloch Representation	42
3.9 Generalization of the Single-Qubit Operation Using Bright-Dark Basis	44
3.10 Electron Spin in a Quantum Dot as a Qubit	47
3.11 Possibility to Realize Geometric Gates Using Nitride Structures	50

4. Conclusions	50
5. References	51
6. Publications and Presentations for this DRI	53
Distribution List	55

List of Figures

Fig. 1	Constant energy surfaces of (a) GaN conduction band at an energy of 750 meV and (b) GaN valence band at an energy of 100 meV of GaN at 300 K.....	3
Fig. 2	Calculated polar optical scattering rate for the nonparabolic conduction band in GaN including the screening effect. The solid lines show the phonon emission rate and the dashed lines show the phonon absorption rate. The electric field of the light is $0.6 \times 10^7 \text{ Vm}^{-1}$ and the excess photon energy is 750 meV.	9
Fig. 3	A schematic representation for time-resolved photoluminescence through optical gating by frequency down-conversion. Excitation laser provides pulses tunable from 3.26 to 5.33 eV, suitable for studying GaN with generated electron-hole pairs up to 10^{20} cm^{-3}	12
Fig. 4	Calculated time evolution of the electron (a) and hole (b) number density functions at room temperature	13
Fig. 5	(a) Calculated effect of scattering mechanisms on the integrated density of electrons in GaN vs. electric field of the external light at 300 K when the excess photon energy is 50 meV. (b) Calculated effect of scattering mechanisms on the integrated density of electrons in GaN vs. electric field of the pulse at 300 K when the excess photon energy is 750 meV.	15
Fig. 6	Calculated normalized electron density vs. time at room temperature in GaN. The electric field of the light pulse is 10^8 Vm^{-1} for 2 values of excess photon energy. These curves have been computed only considering the coherent effects as described in Eqs. 2, 3, and 4, and neglecting the dephasing due to scattering mechanisms. The values are normalized to the maximum of the curve corresponding to 750 meV. ..	16
Fig. 7	Luminescence spectra in GaN at room temperature (300 K) calculated for different energy regions	18
Fig. 8	(a) Luminescence spectra in GaN at 150 K collected at different energy regions. The excess photon energy is 750 meV. (b) Luminescence spectra in GaN at 50 K collected at different energy regions. The excess photon energy is 750 meV. The electric field of the external light pulse is $0.6 \times 10^7 \text{ V m}^{-1}$ in both cases.	19
Fig. 9	Luminescence spectra of GaN at different temperatures collected at band edge energy region. The excess photon energy is 750 meV. (a) shows the experimental results and (b) presents the simulated results for an electric field of the external light pulse of $0.6 \times 10^7 \text{ V m}^{-1}$	20
Fig. 10	Luminescence spectra of GaN at different laser powers collected at band edge energy region. The excess photon energy is 750 meV and the lattice temperature is 150 K. (a) shows the experimental results and (b) presents the simulated results. In (a), E represents the baseline power used in the experiment. In (b), E is the baseline value of electric field employed in the simulation.	21

Fig. 11	Calculated luminescence spectra of GaN at different temperatures collected at band edge energy region. The excess photon energy is 50 meV and the electric field of the external light pulse is $0.6 \times 10^7 \text{ V m}^{-1}$.	22
Fig. 12	The integrated luminescence spectra of GaN collected up to 8 ps vs. normalized laser power collected at band edge energy region. The excess photon energy is 750 meV and the lattice temperature is 150 K.	22
Fig. 13	Calculated polar optical scattering rate for the nonparabolic conduction band in ZnO including the screening effect. The solid lines show the phonon emission rate, and the dashed lines show the phonon absorption rate. The electric field of the light is $0.6 \times 10^7 \text{ Vm}^{-1}$, the excess photon energy is 380 meV, and the lattice temperature is 300 K.	24
Fig. 14	The result of the normalized luminescence intensity from ZnO obtained by experiment (a) and simulation (b). The excess photon energy is 380 meV, and the lattice temperature is 300 K.	25
Fig. 15	The result of the normalized luminescence intensity from ZnO obtained by experiment (dashed line) and simulation (solid line). The excess photon energy is 40 meV, the electric field of the laser pulse is $0.6 \times 10^7 \text{ Vm}^{-1}$, and the lattice temperature is 75 K.	26
Fig. 16	The normalized luminescence intensity from ZnO at different temperature values calculated at band edge energy region. The excess photon energy is 380 meV, and the electric field of the external light pulse is $0.6 \times 10^7 \text{ V m}^{-1}$.	26
Fig. 17	Energy structure of the 3-level system comprising the 2 electron spin states and the trion state	28
Fig. 18	The density plot of the $ 1\rangle$ state population (a) and coherence (b) as a function of the effective pulse area and frequency chirp; $\alpha_p = \alpha_s$, $\delta = 0$. Initially, only the $ 1\rangle$ state is populated.	35
Fig. 19	The density plot of the $ 1\rangle$ state population (a) and coherence (b) as a function of the effective pulse area and frequency chirp; $\alpha_p = \alpha_s$, $\delta\tau_0 = 0.75$. Initially, only the $ 1\rangle$ state is populated.	36
Fig. 20	The Bloch vector representation of the qubit state. Excitation of the qubit by an external field corresponds to the rotation of the B vector about the pseudo field vector, Ω , with components determined by the effective Rabi frequency $\Omega_e(t)$, detuning δ , and the relative phase $\Delta\phi$.	37
Fig. 21	The Bloch vector trajectory for the qubit state $ 0\rangle$ in panel (a) and the qubit state $ 1\rangle$ in panel (b) generated by the sequence of 2 π -pulses with the relative phase $\varphi + \pi$	41
Fig. 22	The Bloch vector trajectory for the qubit state $ i\rangle$ in panel (a) and the qubit state $ -i\rangle$ in panel (b) generated by the sequence of 2 $\pi/2$ -pulses and one π pulse with the relative phase $\varphi + \pi$	42
Fig. 23	Optical selection rules in different bases: (a) the mixed basis is used, where the electron spin states are in the x basis while the trion states are in the z basis; (b) coupling scheme is in the x basis.	48

Fig. 24 The population dynamics of the resonant qubit states with (dotted lines) and without (solid lines) adiabatic elimination of the trion state in the 3-level system. The excitation is generated by the sequence of 2 pairs of π pulses (Gaussian pulse envelopes) with the relative phase $\Delta\varphi = \pi/2$ 49

List of Tables

Table 1	Parameters used in the simulation for GaN	13
Table 2	Parameters used in the simulation.....	24

Acknowledgments

Parts of the work were performed in collaboration with Enrico Bellotti and Sara Shishehchi (Boston University). We thank Michael Wraback for useful discussions.

INTENTIONALLY LEFT BLANK.

1. Objectives

The main objective of this study is to examine coherent quantum effects, such as Rabi oscillations and quantum entanglement in optical spectra of wide-band-gap materials, and to determine the feasibility of fast optical control of quantum states in gallium nitride (GaN) and zinc oxide (ZnO) heterostructures. Because of much stronger exciton-photon interaction in these materials as compared to gallium arsenide (GaAs), it is possible to realize the strong coupling regime at room temperature. We perform an experimental and theoretical study on the dephasing processes in available nitride and zinc oxide materials. This will allow us to take advantage of their unique properties for observing coherent quantum effects at temperatures higher than the cryogenic, at liquid nitrogen temperature and higher. This is a necessary work toward coherent optical control of quantum states at higher temperatures, with ultimately room-temperature coherent control.

1.1 Approach to Achieving the Objectives

We used time-resolved photoluminescence (TRPL) to study the evolution of carrier density and interband polarization in GaN and ZnO materials. Our modeling of ultrafast optical response from semiconductor structures is based on the density matrix formalism. The detailed numerical solution requires a generalized Monte Carlo simulation. An important step toward coherent control of electronic excitations in GaN heterostructures will be an observation of Rabi oscillations in the differential transmission signal. In the wide-band-gap materials like GaN and ZnO, the exciton transition oscillator strength is at least an order of magnitude larger than in GaAs; therefore, the strong coupling regime can be achieved at significantly higher temperatures.

1.2 Progress Made toward Achieving the Director's Research Initiative (DRI) Research Objectives

We performed theoretical and experimental studies of the sub-picosecond kinetics of photoexcited carriers in GaN and ZnO. In the theoretical model, interaction with an external ultrafast laser pulse is treated coherently, and to account for the scattering mechanisms and dephasing processes, a generalized Monte Carlo simulation is used. The scattering mechanisms included are carrier interactions with polar optical phonons and acoustic phonons, and carrier-carrier Coulomb interactions. We studied the effects of various scattering mechanisms on the carrier densities and also presented the temperature and pulse-power-dependent luminescence spectra. The results are presented over a range of temperature,

electric field, and excitation energy of the laser pulse. Here we report the experimental time-resolved photoluminescence studies of GaN and ZnO samples. We also explain the kinetics of the photoexcited carriers by including only carrier-carrier and carrier-phonon interactions and a relatively simple 2-band electronic structure model.

The analysis and modeling of polarization evolution and coherent oscillations in GaN quantum wells will require an inclusion of carrier confinement effects in the quantum kinetic model. Toward this goal, we have included polarization fields and strain in the “k.p model” of electron and hole states in GaN quantum wells as part of our theory of radiative recombination rates in nitride heterostructures. The quantum confinement of electron states is required for effective optical control. Toward that goal, we modeled the evolution of the spin of quantum-confined electrons, providing a clear geometrical interpretation of the qubit dynamics. Using the analytic form of the evolution operator, we proposed a set of single-qubit rotations that is solely based on the geometrical phase. We demonstrated the adiabatic manipulation of a qubit using only the geometric phase. This has some advantages, since it reduces the requirements of perfect tuning of the controlled parameters and is significantly more robust against noise.

2. Temperature Effects in the Kinetics of Photoexcited Carriers in Wide-Band-Gap Semiconductors

The kinetics of photoexcited electrons and holes in GaN and ZnO were studied by sub-picosecond time-resolved photoluminescence. The rise time of the carrier recombination was analyzed as a function of sample temperature, from 14 K to room temperature, and the excitation power. In one set of measurements, the excitation wavelength was chosen such that the excess photon energy was 750 meV above the band gap, well above the polar optical phonon energy. In another set of measurements, the excess photon energy was 50 meV, below the polar optical phonon energy. The goal was to gain a better understanding of the scattering and dephasing processes that accompany the initial photoexcitation of carriers. Results showed little dependence in the rise time on the initial carrier density but strong dependence on the sample temperature, with the rise time increasing by more than 1 order of magnitude as temperature decreases from room temperature down to 14 K. To elucidate the findings, simulations were performed based on a 2-band model and using a Monte Carlo technique. In the model, interaction with an external ultrafast laser pulse is treated coherently, and to account for the scattering mechanisms and dephasing processes, a generalized Monte Carlo simulation is used. The scattering mechanisms included are carrier interactions with polar optical phonons and

acoustic phonons, and carrier-carrier Coulomb interactions. We find reasonable agreement between the simulation and experiment.

2.1 Theoretical Model

In this work we consider a bulk wide-band-gap semiconductor material described by an isotropic parabolic heavy hole band and an isotropic nonparabolic conduction band.¹ Considering the nonparabolicity factor for the conduction band increases the accuracy of the band structure. For the valence band, we just consider the heavy hole band. Within the energy regions considered in this work, holes will be confined to the heavy hole band because of its higher effective mass, which results in a higher density of states compared to that of the light hole band. Since the excitation energies that we consider in this work are lower than the secondary minima, as shown in Fig. 1, the particles will not be accelerated or excited to energy states outside the Γ valley.

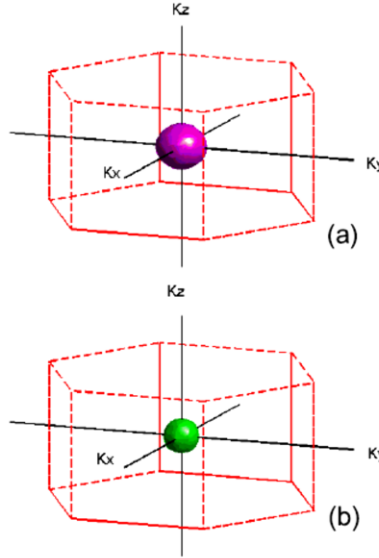


Fig. 1 Constant energy surfaces of (a) GaN conduction band at an energy of 750 meV and (b) GaN valence band at an energy of 100 meV of GaN at 300 K

Figure 1a shows the energy surfaces for the conduction band in GaN at an energy of 750 meV above the conduction band minima, and Fig. 1b shows the energy surfaces for the valence band in GaN at 100 meV below the valence band maxima, calculated using an empirical pseudopotential model. From these figures we can conclude that this simple 2-band model is a good approximation of the realistic electronic structure for the range of energies considered in this work. However, the method can be extended to multiple valleys or full band structures.

The Hamiltonian describing the system contains 2 parts: H_0 , which includes the parts that can be treated exactly using a single particle model, and H_I , which contains various interactions and dephasing processes that will be treated with some level of approximations.

In this work we consider a number of dephasing processes that are due to the interaction of carriers and interband polarization with polar optical and acoustic phonons, and the carrier-carrier interactions via Coulomb potential. We describe the dynamics of the system using the density matrix method.^{2,3} The single particle Hamiltonian that describes the interaction of free carriers with the incoming light field and free phonons is given by

$$H_0 = \sum_k \epsilon_e(k) c_k^\dagger c_k + \sum_k \epsilon_h(k) d_k^\dagger d_k + \sum_k \hbar \omega(q) b_q^\dagger b_q + \sum_k \left[M_k E_0(t) e^{-i\omega_L t} c_k^\dagger d_{-k}^\dagger + M_k^* E_0(t) e^{i\omega_L t} d_{-k} c_k \right], \quad (1)$$

where $\epsilon_e (1 + \alpha\epsilon_e) = \hbar^2 k^2 / (2m_e)$ and $\epsilon_h = \hbar^2 k^2 / (2m_h)$ are the non-parabolic and parabolic energy states for electrons and holes, and m_e and m_h are electron and hole effective masses, respectively. Operators $c_k^\dagger, d_k^\dagger, (c_k, d_k)$ are creation (annihilation) operators of electrons, holes with Fermi anticommutation relations. Operators b_k and b_k^\dagger are phonon operators with Bose commutation relations. ω_q is the phonon frequency, M_k is the interband dipole matrix element, and $E_0(t)$ is the amplitude of the Gaussian-shaped laser pulse with a frequency centered at ω_L and defined as $E_0(t) = E_L \exp(-t^2/\tau^2)$, where E_L is the peak electric field and τ can be related to the full width at half maximum of the measured field intensity by $\tau = \tau' / (2\sqrt{2\ln 2})$. The external light field is treated semi-classically within the rotating wave approximation.⁴ The optical dipole matrix element in the parabolic bands approximation is given by $M_k = d_{cv} (1 + \hbar^2 k^2 / 2m_r E_g)^{-1}$, which can be approximated by a constant, $M_k \approx d_{cv}$, for large band gap values E_g . The reduced mass is defined by $m_r = (m_e^{-1} + m_h^{-1})^{-1}$. The interband electric dipole d_{cv} is related to interband momentum matrix element $d_{cv}/e = \hbar p_{cv} / E_g m_0$ and in the effective mass approximation for 2-band model $d_{cv} = [(-1 + m_0/m_e) / 2E_g m_0]^{1/2}$, from which we obtain in GaN case $d_{cv}/e \approx 2.12 \text{ \AA}$.

To describe the kinetics of the system, we need to obtain the distribution function of the carriers and polarization as well as the rate of change of these functions.

Using the Heisenberg equations of motion, $i\hbar \frac{d}{dt} \hat{O}(t) = [\hat{O}, H]$ for the electron and

hole operators and incorporating appropriate commutation relations, we obtain the equation of motion for particles and polarization that represent the generation rate for a noninteracting system:

$$\left. \frac{df_k^e}{dt} \right|^{(0)} = \left. \frac{df_{-k}^h}{dt} \right|^{(0)} = g_k^{(0)}(t), \quad (2)$$

$$\left. \frac{dp_k}{dt} \right|^{(0)} = \frac{1}{i\hbar} \left[(\varepsilon_e(\mathbf{k}) + \varepsilon_h(-\mathbf{k})) p_k + M_k E_0(t) e^{-i\omega_P t} (1 - f_k^e - f_{-k}^h) \right], \quad (3)$$

with the generation rate

$$g_k^{(0)}(t) = \frac{1}{i\hbar} \left[M_k E_0(t) e^{-i\omega_P t} p_k^* - M_k^* E_0(t) e^{i\omega_P t} p_k \right], \quad (4)$$

where f_k^e , f_k^h and p_k are the distribution functions of electrons, holes, and polarization, respectively:

$f_k^e(t) = \langle c_k^+(t) c_k(t) \rangle$, $f_k^h(t) = \langle d_k^+(t) d_k(t) \rangle$, $p_k(t) = \langle d_{-k}(t) c_k(t) \rangle$, with brackets denoting the expectation value.

Various interactions among the particles are introduced in the model through a perturbing Hamiltonian. For each interaction mechanism, we consider a Hamiltonian H_1^i , where i represents the specific interaction mechanism. In this work we consider polar optical and acoustic phonons, and carrier-carrier interactions. A number of suitable approximations are also included to overcome the difficulties inherent in the many-body nature of these interactions. The carrier-carrier interaction Hamiltonian is given by

$$H_1^{cc} = \sum_{\mathbf{k}, \mathbf{p}, \mathbf{q}} V_q \left[\frac{1}{2} c_k^+ c_p^+ c_{p+q} c_{k-q} + \frac{1}{2} d_k^+ d_p^+ d_{p+q} d_{k-q} - c_k^+ d_{-p}^+ d_{-p+q} c_{k-q} \right], \quad (5)$$

where the first and second terms are the repulsive electron-electron and hole-hole interactions, and the third term is the attractive interaction of electrons and holes, and V_q is the screened Coulomb potential. The first-order approximation in the Heisenberg equations of motion leads to a renormalization of the carrier energies by a self-energy factor and renormalization of the light field by an internal field.² After obtaining the first-order correction, using the Heisenberg equation of motion again, one can derive the equations of the second-order contribution of carrier-carrier interaction. The equation for expectation values of 4 operators involves the strings of 6 operators. We use factorizations to truncate these chains of equations.³

The Markov approximation^{3,4} is used to avoid time integral equations and to neglect the retardation effects. This approximation also implies that the electric field and the distribution functions vary slowly compared to the oscillation of the exponential terms of the laser pulse; therefore, it eliminates the effect of initial

correlations and dynamic memory. Furthermore, the validity of this approach is limited to the range of carrier densities considered in this work and may need to be revised for higher densities. In this work we consider the second-order contribution of the carrier–carrier interaction. The result of the second-order carrier–carrier interaction excluding the Hartree–Fock terms are given in Eqs. 6 and 7, where $\alpha = e, h$:

$$\left. \frac{df_k^\alpha}{dt} \right|^{cc(2)} = - \sum_{k'} [W^{\alpha(cc)}_{k-q,k} f_k^\alpha - W^{i(cc)}_{k,k-q} f_{k-q}^\alpha], \quad (6)$$

$$\left. \frac{dp_k}{dt} \right|^{cc(2)} = - \sum_q [W^p_{k-q,k} p_k - W^p_{k,k-q} p_{k-q}], \quad (7)$$

where the carrier–carrier transition matrices are given by

$$W_{k-q,k}^{\alpha,cc} = \frac{\pi}{\hbar} |V_q|^2 \sum_{\alpha'} \sum_{k'} \mathcal{D}(\varepsilon_{k-q}^\alpha - \varepsilon_k^\alpha + \varepsilon_{k'+q}^{\alpha'} - \varepsilon_{k'}^{\alpha'}) (1 - f_{k-q}^\alpha) [f_{k'}^{\alpha'} (1 - f_{k'+q}^{\alpha'}) - p_{k'+q}^* p_{k'}] + c.c., \quad (8)$$

and the polarization transition matrices are given by

$$W_{k-q,k}^{p,cc} = \frac{\pi}{\hbar} |V_q|^2 \sum_{\alpha,\alpha'} \sum_{k'} \mathcal{D}(\varepsilon_{k-q}^\alpha - \varepsilon_k^\alpha + \varepsilon_{k'+q}^{\alpha'} - \varepsilon_{k'}^{\alpha'}) [-p_{k'+q}^* p_{k'} + f_{k'}^{\alpha'} (1 - f_{k'+q}^{\alpha'}) (1 - f_{k-q}^\alpha) + f_{k-q}^\alpha f_{k'+q}^{\alpha'} (1 - f_{k'}^{\alpha'})]. \quad (9)$$

The function $\mathcal{D}(\epsilon)$ is defined as follows:

$$\mathcal{D}(\omega) \equiv \frac{1}{i\pi} \frac{\mathcal{P}}{\omega} + \delta(\omega), \quad (10)$$

where \mathcal{P} denotes principal value.

Because of the presence of free carriers, the Coulomb potential is screened. We use a static screening potential

$$V_q = \frac{e^2}{\varepsilon_0 \varepsilon_s} \frac{1}{q^2 + \kappa^2}, \quad (11)$$

where ε_0 and ε_s are the vacuum permittivity and static dielectric constant, respectively. The screening wave vector is calculated according to the following equation:

$$\kappa^2 = -\frac{e^2}{\epsilon_s \epsilon_0 V} \sum_{k,\alpha} \left(\frac{\partial \epsilon_\alpha(k)}{\partial k} \right)^{-1} \left(\frac{\partial f_k^\alpha}{\partial k} \right), \quad (12)$$

where $\epsilon(k)$ is the carrier energy state, and V is the volume of the material.

Besides the interaction of carriers with each other, in this work we take into account the interaction with polar optical and acoustic phonons as well. The structure of the Hamiltonian describing these interactions is independent of the type of the phonon branch. The only difference is the interaction matrix element that describes the type of lattice deformation, in the case of acoustic phonons, and the long-range electric field when polar optical modes are considered. The Hamiltonian that describes the carrier-phonon interaction is

$$H_1^{cp} = \sum_{k,q} \left[\gamma_q^e c_{k+q}^\dagger b_q c_k + \gamma_q^{e*} c_k^\dagger b_q^\dagger c_{k+q} + \gamma_q^h d_{k+q}^\dagger b_q d_k + \gamma_q^{h*} d_k^\dagger b_q^\dagger d_{k+q} \right], \quad (13)$$

where $\gamma_q^{e,h}$ is the interaction matrix element. Because of the opposite charge of electrons and holes, the matrix elements in the case of a polar interaction are $\gamma_q^e = -\gamma_q^h = \gamma_q$. The procedure of obtaining the second-order contribution of the carrier-phonon interaction to the equations of motion is similar to that of carrier-carrier interaction. We derive Heisenberg equations of motion using the Markov approximation. The second-order contribution to the equations of motion, excluding the internal field terms, is the same as Eqs. 6 and 7; however, instead of $W^{e,h(cc)}$ and $W^{p(cc)}$, the contribution of phonons $W^{e,h(cp)}$ and $W^{p(cp)}$ must be substituted. The carrier-phonon scattering rates are given by

$$W_{k-q,k}^{\alpha,(cp)} = \frac{2\pi}{\hbar} \sum_{\pm} |\gamma_q|^2 \delta(\epsilon_k^\alpha - \epsilon_{k-q}^\alpha \pm \hbar\omega_q) \left(N_q + \frac{1}{2} \pm \frac{1}{2} \right) (1 - f_{k-q}^\alpha), \quad (14)$$

and the polarization transition matrices are given by

$$W_{k-q,k}^{p,(cp)} = \frac{\pi}{\hbar} \sum_{\alpha=e,h} \sum_{\pm} |\gamma_q|^2 \mathcal{D}(\epsilon_k^\alpha - \epsilon_{k-q}^\alpha \pm \hbar\omega_q) \left[\left(N_q + \frac{1}{2} \mp \frac{1}{2} \right) f_{k-q}^\alpha + \left(N_q + \frac{1}{2} \pm \frac{1}{2} \right) (1 - f_{k-q}^\alpha) \right], \quad (15)$$

where N_q is the number of phonons with wave number q at a specific temperature, which is calculated using the Bose-Einstein distribution and ω_q is the phonon frequency.

To obtain the distribution functions, the equations are separated into 2 parts, a coherent part and a dephasing part. The coherent contribution includes the generation equations that are calculated according to Eqs. 3 and 4 for particles and carriers, respectively. The value of the distribution functions in the coherent case

can be obtained by directly integrating the generation equations. A generalized Monte Carlo method,³ which is very similar to the traditional Monte Carlo method, is used to account for the dephasing phenomena. These distribution functions are then used to calculate the luminescence spectrum. The rate of the scattering mechanisms employed in the Monte Carlo procedure is evaluated using the Fermi golden rule. One of the most important scattering mechanisms is the carrier–carrier interaction, especially in GaN with carrier densities as high as 10^{18} cm^{-3} as considered in this work. At this range of carrier densities, the screening effect is essential both for the carrier–carrier scattering and carrier–phonon scattering. In fact, each carrier, while interacting with other carriers through the screened Coulomb potential, is also influenced by the screening potential in its interactions with phonons. Therefore, the carrier–phonon interaction is weakened considerably by the screening potential. The screened carrier–carrier scattering is calculated based on the model,^{5,6} which takes into account the static screening wave vector as shown in Eq. 12. The matrix element of the interaction of the electrons with the polar optical phonons via the Frohlich interaction is as follows⁷:

$$\gamma_q = \frac{e^2 \hbar \omega_{LO}}{\epsilon_0} \left(\frac{1}{\epsilon_\infty} - \frac{1}{\epsilon_s} \right) \frac{q^2}{(q^2 + \kappa^2)^2} I^e(k, k+q), \quad (16)$$

where ϵ_∞ is the high-frequency dielectric constant, q is the wave vector of phonons, ω_{LO} is the polar optical phonon energy, and $I(k, k')$ is the overlap integral for the conduction band.⁷ For the holes, we consider the ordinary polar optical scattering rate for parabolic band structures. The calculated polar optical scattering rate at room temperature, including the effect of screening, is shown in Fig. 2.

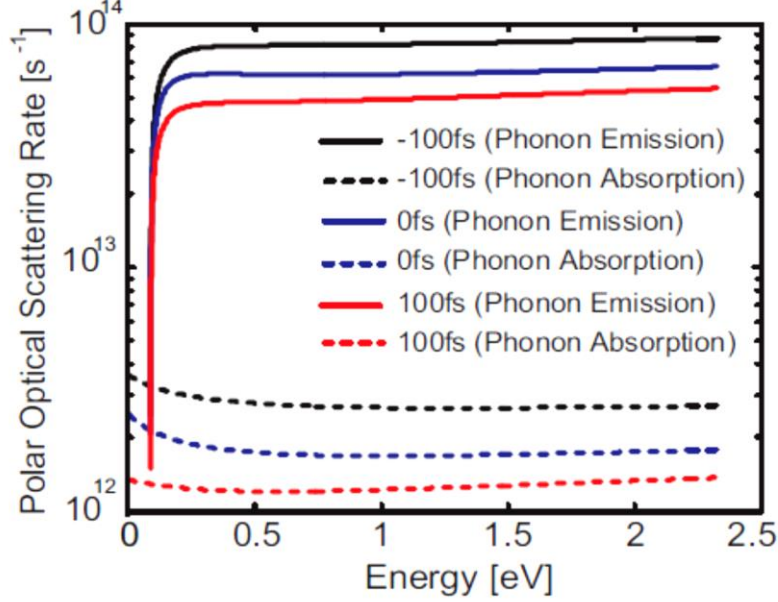


Fig. 2 Calculated polar optical scattering rate for the nonparabolic conduction band in GaN including the screening effect. The solid lines show the phonon emission rate and the dashed lines show the phonon absorption rate. The electric field of the light is $0.6 \times 10^7 \text{ Vm}^{-1}$ and the excess photon energy is 750 meV.

The excess photon energy—the amount of photon energy after subtracting the band gap energy—is 750 meV, and the electric field of the external light is $0.6 \times 10^7 \text{ Vm}^{-1}$. The solid lines show the phonon emission rates, and the dashed lines show the rate for the phonon absorption processes. The black lines (topmost solid and dashed lines) show the calculated scattering rate at -100 fs . At this time, the generation process has just started, and the density of electrons in the system is $8.2 \times 10^{15} \text{ cm}^{-3}$. The blue lines (center solid and dashed lines) show the scattering rates at 0 fs when the maximum of the laser pulse occurs and the density of electrons is $6.1 \times 10^{17} \text{ cm}^{-3}$. Because of the increasing carrier density resulting from a higher generation rate, the screening wave vector changes dynamically as the simulated system evolves. Therefore, the polar optical scattering will be screened, and eventually the scattering rate will decrease. This effect is more pronounced, as shown by the red lines (bottom solid and dashed lines), when the time is 100 fs and more carriers are generated. In this case, the density of electrons is $1.2 \times 10^{18} \text{ cm}^{-3}$, and the electron–phonon scattering rate is at its lowest value. Without the screening effect, the polar optical scattering rate will not change during the simulation run.

The deformation potential acoustic scattering rate for isotropic parabolic and nonparabolic bands are calculated based on the method presented in Jacoboni and Lugli.⁵ For the parabolic bands, only longitudinal modes contribute to the scattering. The scattering rate is calculated considering the acoustic deformation

potentials (D_e and D_h), longitudinal sound velocity (V_L), density of the material (ρ), and the phonon number, nq , which is calculated based on Bose–Einstein distribution. For the nonparabolic conduction band, the average value of the longitudinal and transverse sound velocity (V_T) is used. The transferred energy is calculated based on energy and momentum conservation. The material parameters that have been used in this work are listed in Shishehchi et al.^{1,8}

2.2 Numerical Procedure

This section describes the numerical approach¹ used to evaluate the distribution functions based on the model presented in Section 2.1. Based on this model, the ensemble of the carriers is described by means of a number representation. This means that the number of super particles representing the carriers is defined at each cell in k space; therefore, the occupation of each cell is decreased or increased by one, depending on the mechanism that takes place.⁹ Furthermore, the maximum occupancy of each cell is limited by the density of states. The distribution function is then defined by dividing the occupation number of each cell by the density of state. The distribution functions of electrons and holes are real variables, whereas that of the polarization is complex. Consequently, the magnitude and the phase of polarization are assigned to a 2-vector matrix. The simulation process initiates with the vacuum state of the distribution of carriers and polarization; in other words, the distribution functions and polarization are equal to zero. Subsequently, the ensemble of the carriers and polarization evolves as time elapses as a result of the laser pulse taking the system out of equilibrium.

The simulation period is divided into a number of time steps. At each time step, first the coherent part is calculated. The generation rate for the carriers is evaluated by a direct analytical integration, and the time evolution of the polarization is obtained by integrating the coupled differential Eqs. 2 and 3 employing a Range-Kutta algorithm. The obtained distributions until this point are then transformed into a many-body particle distribution, which can be efficiently used to implement the ensemble Monte-Carlo calculation. Specifically, we use N super-particles for each kinetic variable. These particles are generated randomly according to the distribution function calculated during the coherent part of the time step. Since the polarization distribution function is complex, the phase is discretized according to the complex values of pk . Next, the scattering rates are calculated. Because of the dependence of the screening length on the distribution functions, which are updated at each time step, scattering rates should be recalculated once the new distributions are available. Then, a traditional Monte Carlo simulation is performed using the newly calculated scattering rates. After

each scattering event, the number of super particles in the initial cell is decreased by one, and the number in the final cell is increased by one.

In this work, we also include the effect of the Pauli exclusion principle. Although the Monte Carlo method treats the electrons and holes as semi-classical particles, they should obey the Pauli exclusion principle, especially at high carrier densities where the distribution of the particles is highly influenced by their fermionic properties.¹⁰ After the scattering process, once the final state is defined, a random number between 0 and 1 is generated to evaluate whether the transition is accepted or rejected.¹¹ In this method, the distribution function, f_i , at each cell, i , in the k space is compared to the random number, r . If $r > f_i$, the transition is accepted and the occupancy of that cell is increased by one. Otherwise, the transition is denied and the particle goes through a self-scattering event. Eventually, the distribution function is updated according to the exclusion principle after scattering by each mechanism.

2.3 Experiment

A schematic representation of the experimental setup is shown in Fig. 3. A 250-kHz regeneratively amplified Ti:Sapphire laser produces 150-fs pulses at 800-nm wavelength. Part of this beam is split off, acting as a gating pulse, and the other part pumps an optical parametric amplifier tunable from 760 to 465 nm. Output from the amplifier is again doubled in a nonlinear optical crystal (2Xtal) to produce pulses tunable from 380 to 232.5 nm. The pump pulse, compressed to a width of approximately 80 fs, is focused onto the sample where it photo-excites electron-hole pairs. The luminescence from the sample is collected using nondispersive optics and focused on another nonlinear crystal (NLXtal), where it is mixed with the gating pulse to yield a down-converted signal that is spatially and spectrally separated from the other beam. The down-converted signal is passed through a spectrometer and detected with a photomultiplier tube in photon counting mode. The sample used in this experiment was a 2- μm -thick heteroepitaxial GaN film deposited by metalorganic chemical vapour deposition (MOCVD) with a fully graded aluminum gallium nitride (AlGaN) layer on bulk aluminum nitride (AlN). The arrival time of the near-IR gate pulse relative to the UV photoluminescence maps the TRPL with 350-fs resolution as determined by the group velocity dispersion between the 2 beams in the nonlinear crystal. The energy range of the carrier distribution monitored is a function of the acceptance angle of the phase matching condition in the nonlinear crystal.

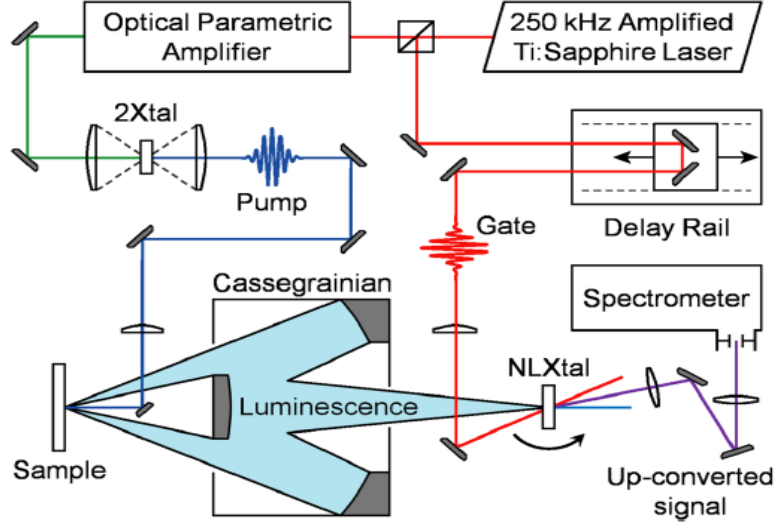


Fig. 3 A schematic representation for time-resolved photoluminescence through optical gating by frequency down-conversion. Excitation laser provides pulses tunable from 3.26 to 5.33 eV, suitable for studying GaN with generated electron-hole pairs up to 10^{20} cm^{-3} .

2.4 Results and Discussion for the Gallium Nitride (GaN) Case

In this section we present and compare the theoretical and the experimental results for the case of GaN. In particular, we will look at the time evolution of the electron and hole densities as a function of the electric field strength and intensity of the external pulse. The material parameters are listed in Table 1. We present the effect of various scattering mechanisms on these results, with particular emphasis on the analysis of the phenomena that lead to the disruption of the coherence in the system. In this context, to highlight the role of polar optical phonon scattering, we consider 2 excitation energies: one with an excess photon energy of 750 meV, which is higher than the polar optical phonon energy (91.2 meV), and the other one with excess photon energy of 50 meV, which is lower than polar optical phonon energy. For the case of excitation with the lower energy, longitudinal optical (LO) phonon emission processes are significantly suppressed and do not drive the energy relaxation in the system. Finally, we consider the calculated luminescence for both values of the excess photon energies. Moreover, we study the effect of temperature on the luminescence spectra and compare it with the measured values.

Table 1 Parameters used in the simulation for GaN

Parameter	Value	Unit
m_e	$0.22m_0$	kg
m_h	$0.88m_0$	kg
ϵ_∞	$5.35\epsilon_0$	F m^{-1}
ϵ_s	$8.9\epsilon_0$	F m^{-1}
$\hbar\omega_0$	91.2	meV
E_g	3.39	eV
M	2.12	\AA
α	0.37	eV^{-1}
D_e	8.3	eV
D_h	22	eV
ρ	6.15	g cm^{-3}
V_L	7.96	10^5cm s^{-1}
V_T	4.13	10^5cm s^{-1}
τ	85	fs

Figure 4a shows the calculated time evolution of the electron number density function at room temperature when the excess photon energy is 750 meV and the electric field of the laser pulse is $0.6 \times 10^7 \text{ V m}^{-1}$. The number density function $n(E)$ is defined as the product of the density of states and the carrier distribution: $n(E) = g(E) f(E)$. Figure 4b provides the same information for holes. The energy in (a) is measured from the bottom of the conduction band, and the energy in (b) is measured from the top of the valence band.

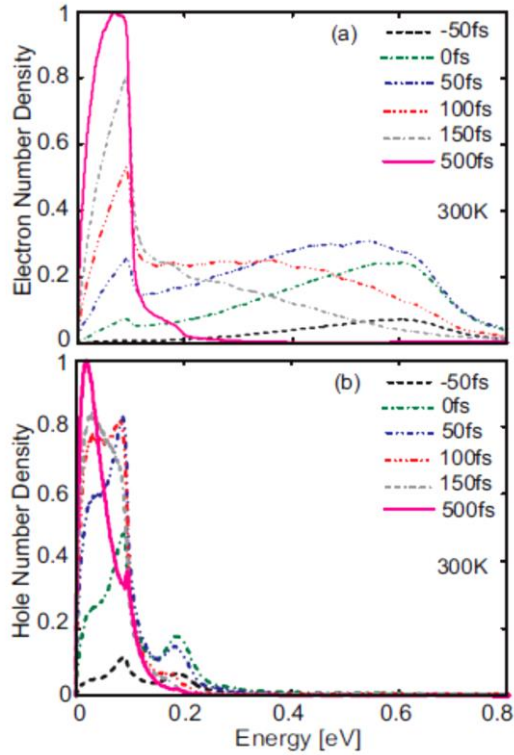


Fig. 4 Calculated time evolution of the electron (a) and hole (b) number density functions at room temperature

The time scale has been chosen so that the peak of the Gaussian laser pulse occurs at 0 fs, and the calculated electric field interaction extends from -200 to 200 fs. The particle distribution results are shown at the instants corresponding to -50 fs, 0 fs, 50 fs, 100 fs, 150 fs, and 500 fs. The dashed black line shows the normalized electron density at -50 fs. At this time step, carriers are being generated and, as the time elapses, the number of the carriers' density increases. Since the excess photon energy of 750 meV is divided between the conduction and valence bands (based on the respective density of states), we observe that the maximum of the electron distribution is below the excess photon energy. For holes, the peak of the distribution occurs just below 200 meV. As the time elapses, the scattering processes relax the carriers' energy and change the shape of the distribution. The dot-dashed green line shows the results at 0 fs—the time at which the laser pulse intensity is maximum. At this time, another peak emerges at an energy of about 91 meV, which corresponds to the optical phonon energy. The peak is due to the polar optical phonon scattering emission mechanism that cannot occur below this energy. At later times, 100 and 150 fs, the shoulder at ≈ 91 meV becomes more and more pronounced. Eventually, at 500 fs when the laser pulse is extinguished, the distribution is completely relaxed and carriers have accumulated in a region close to the band edge energy.

From the time evolution of the carrier number density functions, it is possible to garner additional information on the coherent processes in the system. The coherent effects can be analyzed either as a function of the electric field at a given time or for a given electric field intensity as a function of time. Figures 5a and 5b show the calculated normalized total electron density as a function of the electric field of the external light for the case that the excess photon energy is 50 and 750 meV, respectively. In this case, the lattice temperature is 300 K, and the density values are obtained after the system has reached steady state, long after the laser pulse is finished (1.5 ps). Furthermore, the integrated number of the electrons in the whole k space has been calculated, then the data have been normalized to the maximum value obtained at each field value.

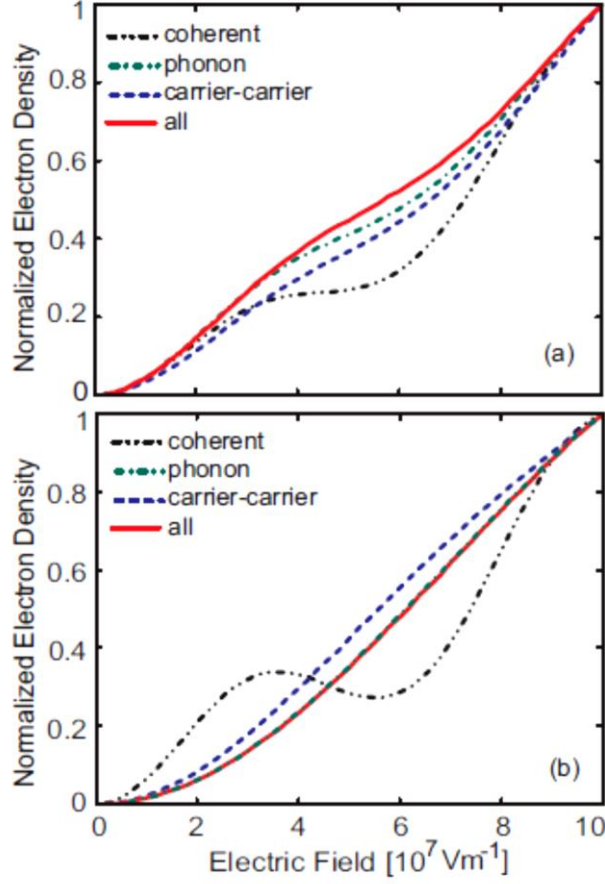


Fig. 5 (a) Calculated effect of scattering mechanisms on the integrated density of electrons in GaN vs. electric field of the external light at 300 K when the excess photon energy is 50 meV. (b) Calculated effect of scattering mechanisms on the integrated density of electrons in GaN vs. electric field of the pulse at 300 K when the excess photon energy is 750 meV.

The various curves in Figs. 5a and 5b illustrate the effect of various scattering mechanisms on the density of the carriers and degree of coherence in the system. The dashed black line shows the coherent case where no dephasing process is included. In this case, the Monte Carlo part of the numerical model is excluded, and the results are obtained by just taking into account the first-order solution of the equations of motion. Since no dephasing process is present, the distribution functions of electrons and holes are highly correlated. Furthermore, Rabi oscillations⁴ can be seen in the result. The oscillation is more pronounced when the excitation energy is higher (750 meV in Fig. 5b). Figure 6 presents the Rabi oscillation in the time domain for the 2 excess energy values.

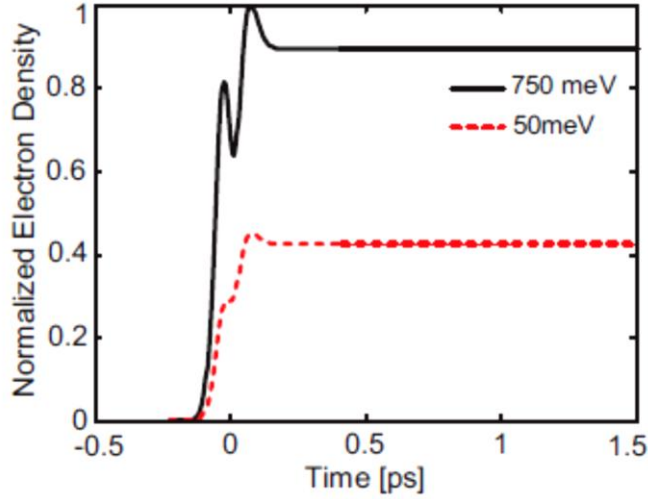


Fig. 6 Calculated normalized electron density vs. time at room temperature in GaN. The electric field of the light pulse is 10^8 Vm^{-1} for 2 values of excess photon energy. These curves have been computed only considering the coherent effects as described in Eqs. 2, 3, and 4, and neglecting the dephasing due to scattering mechanisms. The values are normalized to the maximum of the curve corresponding to 750 meV.

The normalized electron density at room temperature as a function of time for the previous excitation energies when the electric field is equal to 10^8 Vm^{-1} is shown in Fig. 6. The excess photon energies for the solid and dashed lines are 750 and 50 meV, respectively. It can be seen that the Rabi oscillation becomes stronger as the excitation energy increases. Besides the case in which no dephasing is present, Fig. 5 shows the effects of various scattering processes on the coherence in the system. The presence of interactions with phonons and other carriers changes the picture of the correlation between electrons and holes. The dot-dashed green lines in Figs. 5a and 5b show the case that only phonon-scattering mechanisms are included. The phonon-scattering process includes both the polar optical and acoustic scattering mechanisms. In polar optical phonon interaction, the carriers emit or absorb an integer number of phonons, and the distribution relaxes toward lower energy states. Consequently, if the excitation energy is lower than the polar optical energy, the polar optical phonon emission process is less probable. However, acoustic phonon processes, having a much lower energy than polar optical phonons, can occur at any excitation energy. The dashed blue lines represent the case when only the carrier-carrier interaction is included in the system. The role of this process is to basically redistribute the energy in the system; therefore, as a result of this relaxation mechanism, the peaks of the carrier distribution function broaden. Eventually, the solid red line represents the case that all the above mechanisms are included. The broadening effect due to the carrier-carrier scattering is dominant when the excess photon energy is 50 meV

since the polar optical is no longer the dominant energy loss mechanism. To summarize, according to Fig. 5a, for the case that the excess photon energy is less than the polar optical phonon energy, since the polar optical phonon emission is no longer dominant, the total density of electrons, where all the interactions are present, follows the shape of the carrier–carrier dephasing curve. This suggests that in this case, the carrier–carrier scattering mechanism is the dominant process.

However, in Fig. 5b where the photon excess energy is higher than the polar optical phonon energy, polar optical phonon emission is a strong process in relaxing the carriers; therefore, the final density of electrons follows the phonon dephasing curve. In this figure, the electron density values of the carrier–carrier dephasing case at each electric field seem to be larger than the values of the curve where all the scattering rates are included. However, care must be taken in comparison since these are the normalized values. The actual values of the carrier density at each electric field in the case where all the scattering mechanisms are included exceed the values of all the other cases. In fact, the presence of each scattering mechanism affects the distribution of polarization, which has a major role in the carrier generation rate.

To compare the results obtained from the numerical model with the experimental data, we have computed the energy-resolved time-dependent luminescence. To calculate the luminescence at various energies of interest, once the system reaches the steady state condition, we select specific ranges of photon energies. For example, we consider narrow energy regions close to the band gap energy, the polar optical phonon energy, twice the polar optical phonon energy, and other multiples. Subsequently, we multiply the electron and holes at each energy within the narrow band and sum all these partial products over the selected energy region. After that, we normalize the luminescence data to the respective maximum values. Figure 7 shows the calculated energy-resolved time-dependent photoluminescence for the case that the excess photon energy is 750 meV. The electric field of the external pulse is $0.6 \times 10^7 \text{ Vm}^{-1}$ and the lattice temperature is 300 K. The peak of the laser pulse is located at the origin of the time axis, and the time evolution of the carrier ensembles has been collected up to 8 ps.

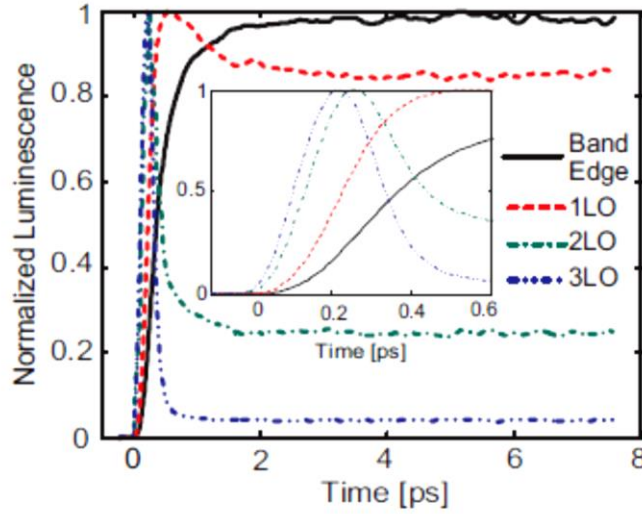


Fig. 7 Luminescence spectra in GaN at room temperature (300 K) calculated for different energy regions

The inset of the figure shows the results up to 0.6 ps where the details and the sequence of the curves are more distinguishable. The solid black line shows the results when the photoluminescence energy is collected at band edge energy, which is the slowest process. The dotted red line, the dot-dashed green line, and the dashed blue line show the results when the selected energy is equal to 1, 2, and 3 polar optical phonon energies (1LO, 2LO, 3LO), respectively. The 3LO case is the fastest process, then the 2LO, and afterwards the 1LO curves reach the steady state.

Figures 8a and 8b present the luminescence results in GaN when the temperature is equal to 50 and 150 K, respectively. The electric field and the excess photon energy are the same as the ones in Fig. 7.

The results clearly show that as the temperature decreases, the rise time increases. More specifically, the rise time for the band edge energy region changes significantly. This is due to the fact that at lower temperatures, the polar optical scattering rate is lower, and therefore this process is weaker in relaxing the carrier distributions.

Although we have endeavored to develop our simulation models to provide the best description of the physical phenomena that emerge from the experiment, a quantitative comparison is not always possible. In fact, the simplified band structure and neglecting the internal field and the imaginary part of the self-energy arising from the second-order correction to the carrier-carrier and carrier-phonon interactions² may lead to simulation results that in some cases can only be in qualitative agreement with the experiment.

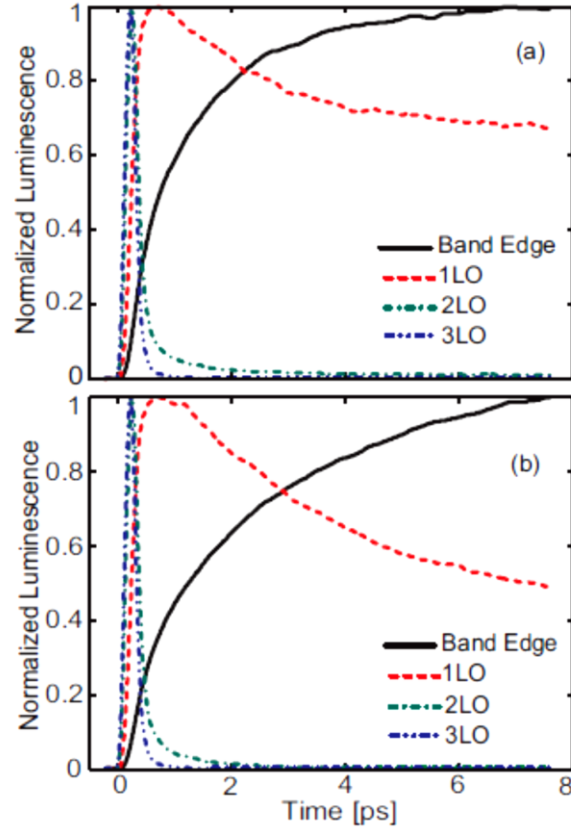


Fig. 8 (a) Luminescence spectra in GaN at 150 K collected at different energy regions. The excess photon energy is 750 meV. (b) Luminescence spectra in GaN at 50 K collected at different energy regions. The excess photon energy is 750 meV. The electric field of the external light pulse is $0.6 \times 10^7 \text{ V m}^{-1}$ in both cases.

Figures 9a and 9b show the results of luminescence for the temperature values ranging from 150 to 300 K obtained by experiment and simulation, respectively, when the excess photon energy is 750 meV. It clearly shows that as the lattice temperature increases, the luminescence rise time decreases.

Because of the specific experimental conditions, it is not always possible to directly correlate the beam power used in the measurements with the electric field magnitude employed in the simulations. In fact, for the model we have employed, as opposed to the case of a semiclassical generation model, the number of generated carriers depends on the interplay between the coherent and dephasing phenomena. Nevertheless, the numerical model predicts the correct trend of the experimental results. It is important to appreciate this point, since the experimental conditions under which the results in Fig. 9a were obtained are not the same as the ones considered in computing the values presented in Fig. 9b.

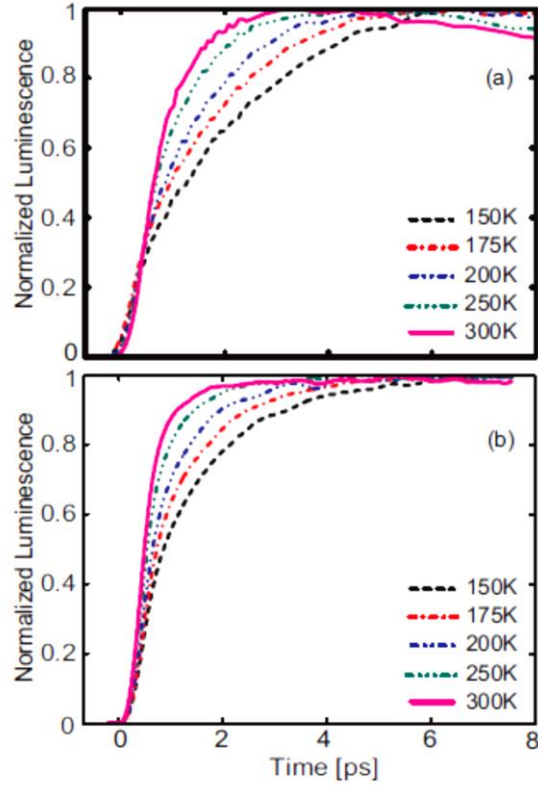


Fig. 9 Luminescence spectra of GaN at different temperatures collected at band edge energy region. The excess photon energy is 750 meV. (a) shows the experimental results and (b) presents the simulated results for an electric field of the external light pulse of $0.6 \times 10^7 \text{ V m}^{-1}$.

In order to show that this is still a valid comparison, even if the power of the beam in the experiment and the electric field magnitude in the numerical model cannot be directly correlated, we have computed the luminescence as a function of the electric field strength. According to the experimental results shown in Fig. 10a, the luminescence rise time is independent of the power of the laser pulse. In both Figs. 10a and 10b, the luminescence results at GaN collected at the band edge energy region are shown over a range of laser pulse powers in which the rise times are approximately the same.

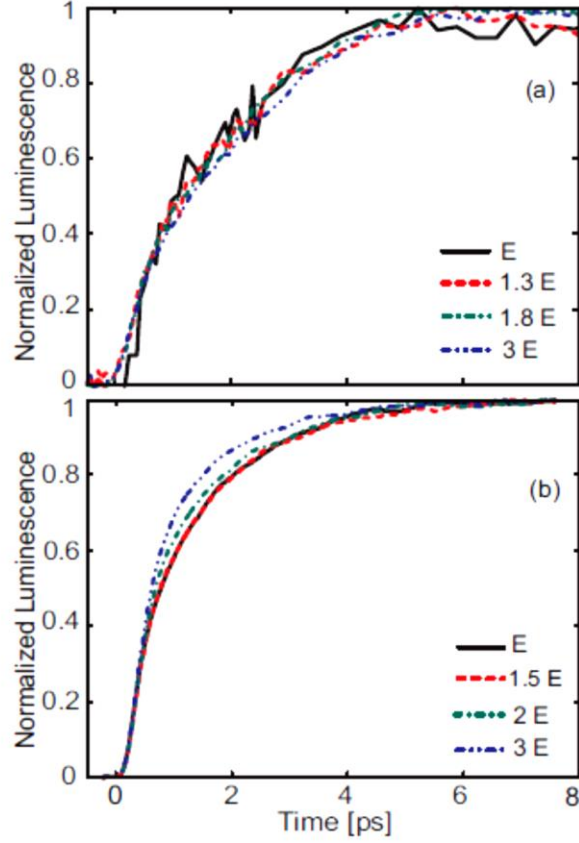


Fig. 10 Luminescence spectra of GaN at different laser powers collected at band edge energy region. The excess photon energy is 750 meV and the lattice temperature is 150 K. (a) shows the experimental results and (b) presents the simulated results. In (a), E represents the baseline power used in the experiment. In (b), E is the baseline value of electric field employed in the simulation.

In Fig. 10, the lattice temperature is 150 K and the excess photon energy is 750 meV. Fig. 10b shows that the numerical simulation results deliver the same trend as the experiment. On the basis of this result, we can justify the comparison made in Figs. 9a and 9b where we presented the temperature-dependent experimental and simulated luminescence rise time. Figure 11 shows the luminescence spectra collected at the band edge energy region when the electric field of the light is $0.6 \times 10^7 \text{ Vm}^{-1}$ and the excess photon energy is 50 meV. The results are just for the band edge energy because the higher energies are less important—in this case, the excess photon energy is lower than the polar optical phonon energy.

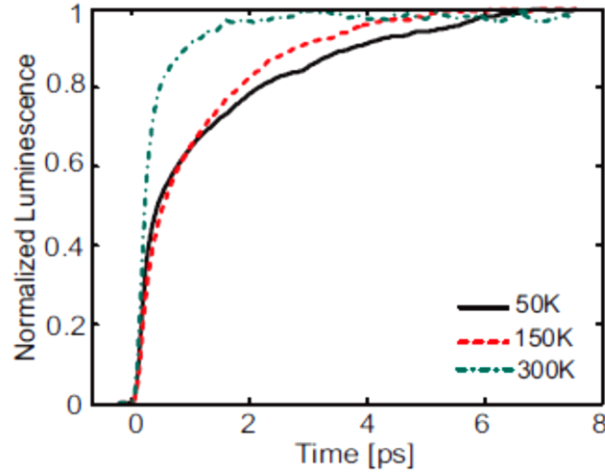


Fig. 11 Calculated luminescence spectra of GaN at different temperatures collected at band edge energy region. The excess photon energy is 50 meV and the electric field of the external light pulse is $0.6 \times 10^7 \text{ V m}^{-1}$.

The solid black line shows the results when the temperature is 50 K, the dashed red line shows the results when the temperature is 150 K, and the dot-dashed green line shows the results when the temperature is 300 K. As seen in the figure, when the temperature decreases, the rise time of the luminescence spectrum increases. Figure 12 shows the results of the integrated luminescence spectrum in GaN collected up to 8 ps at the band edge energy region. The lattice temperature is 150 K, and the excess photon energy is 750 meV. The results are shown versus the normalized power of the laser pulse. The solid line shows the results of the theory, and the marker points show those of experiment. The figure clearly shows a reasonable agreement in the results. As the power increases, because of the generation of more carriers, the intensity of the luminescence spectrum increases.

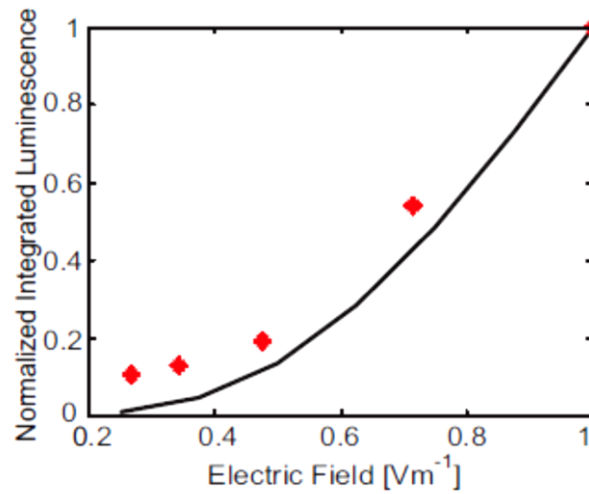


Fig. 12 The integrated luminescence spectra of GaN collected up to 8 ps vs. normalized laser power collected at band edge energy region. The excess photon energy is 750 meV and the lattice temperature is 150 K.

2.5 Summary for Gallium Nitride (GaN) Experiments and Modeling

We presented a theoretical and experimental study of the subpicosecond kinetics of photoexcited carriers in GaN. We considered a bulk GaN model with an isotropic parabolic heavy hole band and an isotropic nonparabolic conduction band. In the theoretical model, interaction with an external ultrafast laser pulse is treated coherently, and to include the scattering mechanisms and dephasing processes, a generalized Monte Carlo simulation is used.

The scattering mechanisms included are carrier interactions with polar optical phonons and acoustic phonons, and carrier–carrier Coulomb interactions. The results of the integrated density of electrons are shown for 2 different excess photon energies. In the case where the excess photon energy (50 meV) is less than the polar optical phonon energy, carrier–carrier scattering is the dominant process. However, when the excess photon energy (750 meV) is greater than optical phonon energy, the polar optical phonon scattering is the most significant relaxing process. Besides the carrier densities, temperature-dependent luminescence spectra have been studied. We showed that for all values of the excess photon energies, as the temperature decreases, the luminescence rise time increases. This effect is due to the lower polar optical scattering rate, which results in the fact that this process is no longer strong enough to relax the carriers. For comparison, we also report the experimental time-resolved photoluminescence studies on GaN samples. In conclusion, we have shown that we can explain the kinetics of the photoexcited carriers in GaN by including only carrier–carrier and carrier–phonon interactions and a relatively simple 2-band electronic structure model. Furthermore, we have presented a detailed analysis of the effect of a different dephasing mechanism on the carrier kinetics. Finally, we have experimentally measured and simulated using our theoretical model the temperature and pulse power dependence of the photoluminescence spectra.

2.6 Results and Discussion for the Zinc Oxide (ZnO) Case

In this section, we present and compare the normalized luminescence intensity results obtained by theory and experiment in the case of ZnO. More specifically, we compare the luminescence rise times and the effect of temperature on them. The results are obtained in a range of excitation energies and temperature values. The material parameters for ZnO are given in Table 2.

The calculated polar optical scattering rates for electrons are shown in Fig. 13, when the electric field of the light is $0.6 \times 10^7 \text{ Vm}^{-1}$, the excess photon energy is 380 meV, and the lattice temperature is 300 K.

Table 2 Parameters used in the simulation

Parameter	Value	Unit
m_e	$0.21m_0$	kg
m_h	$0.59m_0$	kg
ϵ_∞	$4.07\epsilon_0$	Fm^{-1}
ϵ_s	$8.27\epsilon_0$	Fm^{-1}
$\hbar\omega_0$	72.9	meV
E_g	3.373	eV
M	2	\AA
α	0.4	eV^{-1}
D_e	7.5	eV
D_h	22	eV
ρ	6.10	g cm^{-3}
V_L	6.59	10^5 cm s^{-1}
V_T	2.79	10^5 cm s^{-1}
τ	85	fs

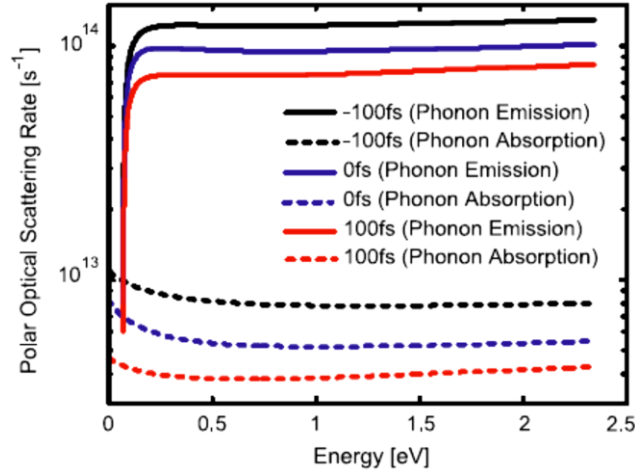


Fig. 13 Calculated polar optical scattering rate for the nonparabolic conduction band in ZnO including the screening effect. The solid lines show the phonon emission rate, and the dashed lines show the phonon absorption rate. The electric field of the light is $0.6 \times 10^7 \text{ Vm}^{-1}$, the excess photon energy is 380 meV, and the lattice temperature is 300 K.

Figures 14a and 14b show the results of the normalized luminescence intensity obtained by experiment and simulation, respectively. The excess photon energy is 380 meV, and the lattice temperature is 300 K. Different curves show the energy regions where the luminescence has been obtained, and each curve is normalized to its maximum value. The solid black line shows the result of the luminescence obtained for photon energies near the band edge transition. The dashed red line, dot-dashed green line, and double-dot-dashed blue line show the same results obtained at 0.5, 1, and 1.5 polar optical phonon energy in excess of the band edge optical energy transition, respectively.

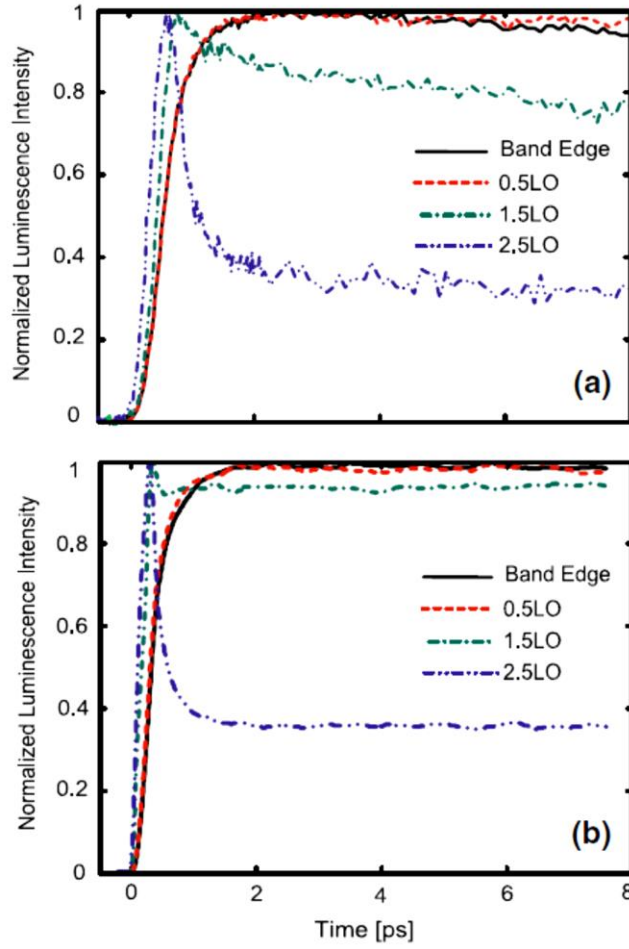


Fig. 14 The result of the normalized luminescence intensity from ZnO obtained by experiment (a) and simulation (b). The excess photon energy is 380 meV, and the lattice temperature is 300 K.

Figure 15 shows the result of the normalized luminescence intensity from ZnO obtained at the band edge energy region. The dashed line represents the experimental result, and the simulated result is shown by the solid line. In this case, the excess photon energy is 40 meV, and the lattice temperature is 75 K.

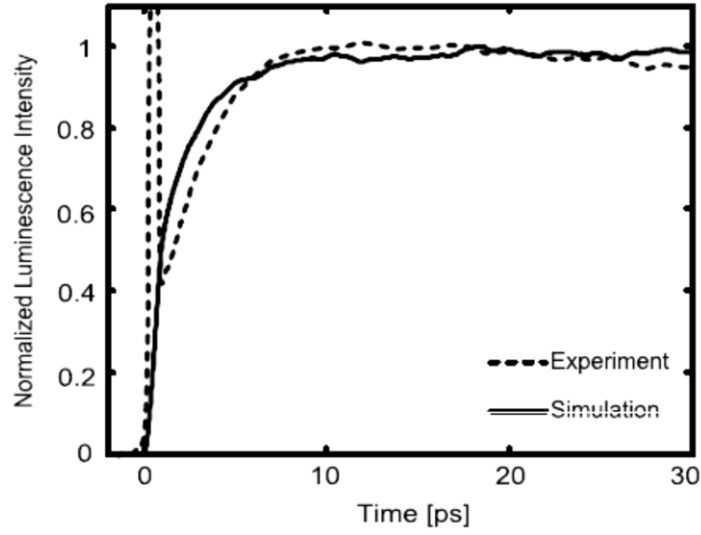


Fig. 15 The result of the normalized luminescence intensity from ZnO obtained by experiment (dashed line) and simulation (solid line). The excess photon energy is 40 meV, the electric field of the laser pulse is $0.6 \times 10^7 \text{ Vm}^{-1}$, and the lattice temperature is 75 K.

Besides the results of the rise time, we also investigated the effect of temperature on the rise time. Figure 16 shows the results of the normalized luminescence intensity, when the excess photon energy is 380 meV, calculated at the band edge energy region over a range of lattice temperature values from 150 to 300 K. It clearly shows that, as the lattice temperature increases, the luminescence rise time decreases. This is because at lower temperatures, the polar optical scattering rate is weaker than at room temperature and, therefore, this process is not as effective in relaxing the carrier distributions.

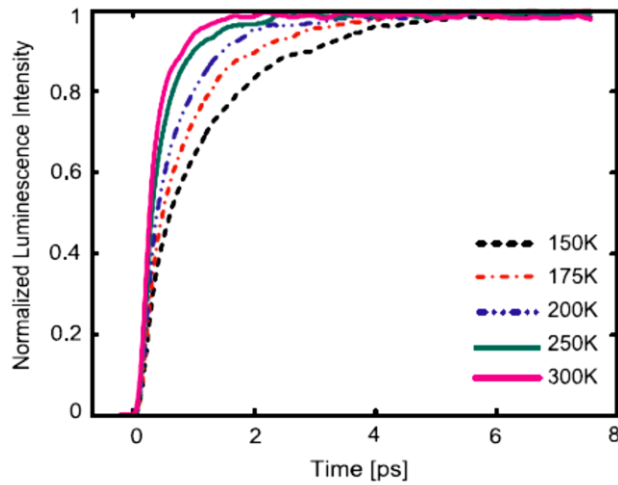


Fig. 16 The normalized luminescence intensity from ZnO at different temperature values calculated at band edge energy region. The excess photon energy is 380 meV, and the electric field of the external light pulse is $0.6 \times 10^7 \text{ V m}^{-1}$.

In this study we considered bulk ZnO modeled by an isotropic parabolic heavy hole band and an isotropic nonparabolic conduction band. In the theoretical model, interaction with an external ultrafast laser pulse is treated coherently, and the scattering mechanisms and the dephasing processes are taken into account through a generalized Monte Carlo simulation. The scattering mechanisms included are carrier interactions with polar optical phonons and acoustic phonons, and carrier–carrier Coulomb interactions. The results of the calculated normalized luminescence intensity from ZnO at 2 excitation energies and lattice temperature values are in good agreement with those of the experimental study obtained by the time-resolved photoluminescence method. We also presented the calculated results of the temperature-dependent luminescence intensity. As a conclusion, as the temperature decreases, the luminescence rise time increases. This effect is due to the lower polar optical scattering rate, which results because this process is no longer strong enough to relax the carriers.

In conclusion, we have shown that we can explain the dynamics of the photoexcited carriers in ZnO by including only carrier–carrier and carrier–phonon interactions and a relatively simple 2-band electronic structure model.

3. Geometric Single-Qubit Quantum Gates for an Electron Spin in a Quantum Dot

We propose a scheme to perform arbitrary unitary operations on a single electron-spin qubit in a quantum dot. The design is solely based on the geometrical phase that the qubit state acquires after a cyclic evolution in the parameter space. The scheme uses ultrafast linearly chirped pulses, providing adiabatic excitation of the qubit states, and the geometric phase is fully controlled by the relative phase between pulses. The analytic expression of the evolution operator for the electron spin in a quantum dot, which provides a clear geometrical interpretation of the qubit dynamics, is obtained. Using parameters of InGaN/GaN and GaN/AlN quantum dots, we provide an estimate for the time scale of the qubit rotations and parameters of the external fields.

3.1 Introduction

The electron spin in a single quantum dot is one of the perspective realizations of a qubit for the implementation of a quantum computer. During the last decade, several control schemes to perform single gate operations on a single quantum dot spin have been reported.^{12–15} Here we propose a scheme that allows performing ultrafast arbitrary unitary operations on a single qubit represented by the electron spin. The idea of geometric manipulation of the qubit wave function has been

recently developed into a new research direction called geometric quantum computing.^{16–18} The main motivation of this development is the robustness of geometric quantum gates against noise.^{19,20} In this report, we demonstrate how to use the geometric phase, which the Bloch vector gains along the cyclic path, to prepare an arbitrary state of a single qubit. We show that the geometrical phase is fully controllable by the relative phase between the external fields. We also discuss the realistic implementation of the proposed design using the electron spin in a charged quantum dot as an example of a qubit.

3.2 General Equations of Motion

Let us consider the coherent Raman excitation in the 3-level Λ -type system consisting of the 2 lowest states of electron spin $|0\rangle \equiv |-X\rangle$ and $|1\rangle \equiv |X\rangle$ coupled through an intermediate trion state $|T\rangle$ consisting of 2 electrons and a heavy hole²¹ (Fig. 17).

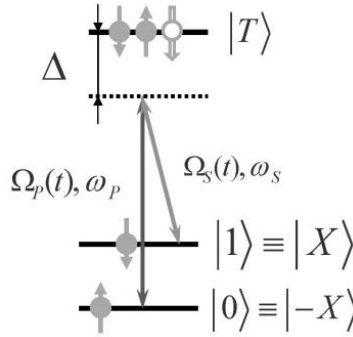


Fig. 17 Energy structure of the 3-level system comprising the 2 electron spin states and the trion state

We assume that the trion state is far off-resonance with the external fields to ensure that decoherence on the trion-qubit transitions can be neglected. The electron spin states are split by an external magnetic field; the separation energy is $\hbar\omega_e$. The total wave function of the system

$$|\Psi(t)\rangle = a_0(t)|0\rangle + a_1(t)|1\rangle + b(t)|T\rangle, \quad (17)$$

where $a_{0,1}(t)$ and $b(t)$ are the probability amplitudes, is governed by the time-dependent Schrödinger equation with the Hamiltonian

$$\mathbf{H} = \hbar \begin{pmatrix} 0 & 0 & -(\Omega_p(t) + \bar{\Omega}_s(t)) \\ 0 & \omega_e & -(\bar{\Omega}_p(t) + \Omega_s(t)) \\ -(\Omega_p(t) + \bar{\Omega}_s(t)) & -(\bar{\Omega}_p(t) + \Omega_s(t)) & \omega_T \end{pmatrix}, \quad (18)$$

where

$$\Omega_{P,S}(t) = \Omega_{P0,S0}(t) \cos[\omega_{P,S}t + \phi_{P,S}(t)],$$

$$\bar{\Omega}_{P,S}(t) = \bar{\Omega}_{P0,S0}(t) \cos[\omega_{P,S}t + \phi_{P,S}(t)],$$

$$\Omega_{P0,S0}(t) = \mu_{0T,T1} E_{P,S}(t) / \hbar, \text{ and}$$

$$\bar{\Omega}_{P0,S0}(t) = \mu_{1T,T0} E_{P,S}(t) / \hbar \text{ are the Rabi frequencies;}$$

$$\mu_{0T,T1} \text{ are the dipole moments;}$$

$$E_{P,S}(t) \text{ are the pulse envelopes;}$$

$$\omega_{P,S} \text{ are the center frequencies;}$$

$$\phi_{P,S}(t) \text{ are the time-dependent phases; and}$$

$$\hbar\omega_T \text{ is the energy of the trion state.}$$

We are considering here a case of linearly chirped pulses such that

$$\phi_{P,S}(t) = \phi_{P,S} + \alpha_{P,S} t^2 / 2, \quad (19)$$

where $\phi_{P,S}$ are the initial phases and $\alpha_{P,S}$ are the chirps of the pulses.

Using transformation $|\Psi(t)\rangle = \mathbf{U}_{RWA} |\tilde{\Psi}(t)\rangle$, where

$$\mathbf{U}_{RWA} = \begin{pmatrix} 1 & 0 & 0 \\ 0 & e^{i(\omega_S - \omega_P)t} & 0 \\ 0 & 0 & e^{-i\omega_P t} \end{pmatrix}, \quad (20)$$

$$\mathbf{U}_{RWA}^{-1} = \begin{pmatrix} 1 & 0 & 0 \\ 0 & e^{-i(\omega_S - \omega_P)t} & 0 \\ 0 & 0 & e^{i\omega_P t} \end{pmatrix}, \quad (21)$$

we make the rotating wave approximation (RWA) by neglecting the rapidly oscillating terms with frequency $2\omega_S, 2\omega_P$ and $\omega_S + \omega_P$. In the RWA, the Hamiltonian has the following form:

$$\begin{aligned}
\mathbf{H} &= \mathbf{U}_{RWA}^{-1} \mathbf{H} \mathbf{U}_{RWA} - i\hbar \mathbf{U}_{RWA}^{-1} \dot{\mathbf{U}}_{RWA} \\
&= -\frac{\hbar}{2} \begin{pmatrix} 0 & 0 & \Omega_{P+} + \bar{\Omega}_{S+} e^{-i\Delta\omega t} \\ 0 & -2\omega_e & \bar{\Omega}_{P+}(t) e^{i\Delta\omega t} + \Omega_{S+} \\ \Omega_{P+}^* + \bar{\Omega}_{S+}^* e^{i\Delta\omega t} & \bar{\Omega}_{P+}^* e^{-i\Delta\omega t} + \Omega_{S+}^* & -2\omega_T \end{pmatrix} \\
&\quad + \hbar \begin{pmatrix} 0 & 0 & 0 \\ 0 & -\Delta\omega & 0 \\ 0 & 0 & -\omega_P \end{pmatrix} \\
&= -\frac{\hbar}{2} \begin{pmatrix} 0 & 0 & \Omega_{P+} + \bar{\Omega}_{S+} e^{-i\Delta\omega t} \\ 0 & 2(\Delta\omega - \omega_e) & \bar{\Omega}_{P+}(t) e^{i\Delta\omega t} + \Omega_{S+} \\ \Omega_{P+}^* + \bar{\Omega}_{S+}^* e^{i\Delta\omega t} & \bar{\Omega}_{P+}^* e^{-i\Delta\omega t} + \Omega_{S+}^* & -2\Delta_P \end{pmatrix},
\end{aligned} \tag{22}$$

where

$$\Delta_P = \omega_T - \omega_P, \Delta\omega = \omega_P - \omega_S,$$

$$\Omega_{P+} = \Omega_{P0}(t) e^{i\phi_P(t)}, \Omega_{S+} = \Omega_{S0}(t) e^{i\phi_S(t)},$$

$$\bar{\Omega}_{P+} = \bar{\Omega}_{P0}(t) e^{i\phi_P(t)}, \text{ and}$$

$$\bar{\Omega}_{S+} = \bar{\Omega}_{S0}(t) e^{i\phi_S(t)}.$$

Assuming large detunings of the pump and Stokes field frequencies from the transition frequencies to the trion state, we apply the adiabatic elimination of the trion state. In that case, $\dot{\tilde{b}} \approx 0$ and we find

$$\tilde{b} = \frac{1}{2\Delta_P} \left[\left(\Omega_{P+}^* + \bar{\Omega}_{S+}^* e^{i\Delta\omega t} \right) \tilde{a}_0(t) + \left(\bar{\Omega}_{P+}^* e^{-i\Delta\omega t} + \Omega_{S+}^* \right) \tilde{a}_1(t) \right]. \tag{23}$$

Substituting Eq. 23 into equations for $a_{0,1}$ after some algebra, we obtain the following form of the Hamiltonian for the effective 2-level system:

$$\tilde{\mathbf{H}} = -\frac{\hbar}{2} \begin{pmatrix} \Omega_{ac0}(t) & \Omega_{eff}(t) \\ \Omega_{eff}^*(t) & \Omega_{ac1}(t) - 2\delta \end{pmatrix}, \tag{24}$$

where $\delta = \omega_e - \Delta\omega$,

$$\Omega_{ac0}(t) = \frac{1}{2\Delta_P} (\Omega_{P0}^2(t) + \bar{\Omega}_{S0}^2(t) + 2\Omega_{P0}(t)\bar{\Omega}_{S0}(t) \cos[\phi_P(t) - \phi_S(t) + \Delta\omega t]), \tag{25}$$

$$\Omega_{ac1}(t) = \frac{1}{2\Delta_P} (\Omega_{S0}^2(t) + \bar{\Omega}_{P0}^2(t) + 2\Omega_{S0}(t)\bar{\Omega}_{P0}(t) \cos[\phi_P(t) - \phi_S(t) + \Delta\omega t]), \tag{26}$$

$$\begin{aligned}\Omega_{eff}(t) = & \frac{e^{-i\Delta\omega t}}{2\Delta_P} \left(\Omega_{P0}(t)\bar{\Omega}_{P0}(t) + \Omega_{S0}(t)\bar{\Omega}_{S0}(t) \right. \\ & \left. + \Omega_{P0}(t)\Omega_{S0}(t)e^{i[\phi_P(t)-\phi_S(t)+\Delta\omega t]} + \bar{\Omega}_{P0}(t)\bar{\Omega}_{S0}(t)e^{-i[\phi_P(t)-\phi_S(t)+\Delta\omega t]} \right).\end{aligned}\quad (27)$$

Since $\Omega_{P0}(t)\Omega_{S0}(t) = \bar{\Omega}_{P0}(t)\bar{\Omega}_{S0}(t)$, we have

$$\begin{aligned}\Omega_{eff}(t) = & \frac{e^{-i\Delta\omega t}}{2\Delta_P} \left(\Omega_{P0}(t)\bar{\Omega}_{P0}(t) + \Omega_{S0}(t)\bar{\Omega}_{S0}(t) \right. \\ & \left. + 2\Omega_{P0}(t)\Omega_{S0}(t)\cos[\phi_P(t)-\phi_S(t)+\Delta\omega t] \right).\end{aligned}\quad (28)$$

Making the transformation $|\tilde{\Psi}(t)\rangle = \mathbf{U}|\bar{\Psi}(t)\rangle$, with

$$\mathbf{U} = \begin{pmatrix} e^{-i\delta t/2+i\int_{-\infty}^t dt' \Omega_{st}(t')} & 0 \\ 0 & e^{-i\delta t/2+i\int_{-\infty}^t dt' \Omega_{st}(t')} \end{pmatrix} = e^{-i\delta t/2+i\int_{-\infty}^t dt' \Omega_{st}(t')} \mathbf{I}, \quad (29)$$

where $\Omega_{st}(t) = (\Omega_{ac0}(t) + \Omega_{ac1}(t))/4$, we can rewrite Eq. 24 in a more symmetric form. In the new basis, the Hamiltonian takes the form

$$\begin{aligned}\bar{\mathbf{H}} &= \mathbf{U}^{-1}\tilde{\mathbf{H}}\mathbf{U} - i\hbar\mathbf{U}^{-1}\dot{\mathbf{U}} = \tilde{\mathbf{H}} + \hbar(\Omega_{st}(t) - \delta/2) \mathbf{I} \\ &= -\frac{\hbar}{2} \begin{pmatrix} \delta + \Omega_{dif}(t) & \Omega_{eff}(t) \\ \Omega_{eff}^*(t) & -\delta - \Omega_{dif}(t) \end{pmatrix},\end{aligned}\quad (30)$$

where $\Omega_{dif}(t) = (\Omega_{ac0}(t) - \Omega_{ac1}(t))/2$.

Taking into account the exact time dependence of the phases in Eq. 19, we apply another transformation $|\bar{\Psi}(t)\rangle = \mathbf{U}_F|\tilde{\Psi}(t)\rangle$, with

$$\mathbf{U}_F = \begin{pmatrix} e^{i\zeta t^2/4} & 0 \\ 0 & e^{-i\zeta t^2/4} \end{pmatrix} = e^{i\zeta \frac{t^2}{4} \sigma_z}, \quad (31)$$

where $\zeta = \alpha_P - \alpha_S$. Therefore, in the field interaction representation the Hamiltonian takes the following form:

$$\begin{aligned}
\tilde{\mathbf{H}} &= \mathbf{U}_F^{-1} \bar{\mathbf{H}} \mathbf{U}_F - i\hbar \mathbf{U}_F^{-1} \dot{\mathbf{U}}_F \\
&= -\frac{\hbar}{2} \begin{pmatrix} \delta + \Omega_{dif}(t) & \Omega_{eff}(t)e^{-i\zeta t^2/4} \\ \Omega_{eff}^*(t)e^{i\zeta t^2/4} & -\delta - \Omega_{dif}(t) \end{pmatrix} + \frac{\hbar}{2} \begin{pmatrix} \zeta t & 0 \\ 0 & -\zeta t \end{pmatrix} \\
&= -\frac{\hbar}{2} \begin{pmatrix} \delta - \zeta t + \Omega_{dif}(t) & \Omega_{eff}(t)e^{-i\zeta t^2/4} \\ \Omega_{eff}^*(t)e^{i\zeta t^2/4} & -\delta + \zeta t - \Omega_{dif}(t) \end{pmatrix} \\
&= -\frac{\hbar}{2} \begin{pmatrix} \delta(t) & \bar{\Omega}_{eff}(t)e^{i\Delta\phi} \\ \bar{\Omega}_{eff}^*(t)e^{-i\Delta\phi} & -\delta(t) \end{pmatrix},
\end{aligned} \tag{32}$$

where $\delta(t) = \delta + (\alpha_S - \alpha_P)t + \Omega_{dif}(t)$, $\Delta\phi = \phi_P - \phi_S$, and

$$\begin{aligned}
\bar{\Omega}_{eff}(t) &= \frac{\Omega_{P0}(t)\Omega_{S0}(t)}{2\Delta_P} \left(1 + \frac{\Omega_{P0}(t)\bar{\Omega}_{P0}(t) + \Omega_{S0}(t)\bar{\Omega}_{S0}(t)}{\Omega_{P0}(t)\Omega_{S0}(t)} e^{-i[\Delta\phi + \Delta\omega t + \zeta t^2/2]} \right. \\
&\quad \left. + \frac{\bar{\Omega}_{P0}(t)\bar{\Omega}_{S0}(t)}{\Omega_{P0}(t)\Omega_{S0}(t)} e^{-2i[\Delta\phi + \Delta\omega t + \zeta t^2/2]} \right).
\end{aligned} \tag{33}$$

In general, the differential AC Stark shift, $\Omega_{dif}(t)$, is not zero and has to be taken into account. Using the definition of the Rabi frequency, we can rewrite Eqs. 25 and 26 in the form

$$\Omega_{ac0}(t) = \frac{\mu_{0T}^2}{2\hbar^2\Delta_P} (E_P^2(t) + E_S^2(t) + 2E_P(t)E_S(t)\cos[\phi_P(t) - \phi_S(t) + \Delta\omega t]), \tag{34}$$

$$\Omega_{ac1}(t) = \frac{\mu_{1T}^2}{2\hbar^2\Delta_P} (E_P^2(t) + E_S^2(t) + 2E_P(t)E_S(t)\cos[\phi_P(t) - \phi_S(t) + \Delta\omega t]). \tag{35}$$

In the case when $\mu_{0T} \approx \mu_{1T}$, the AC Stark shifts are the same for both qubit states, so that $\Omega_{dif}(t) = 0$, and we have

$$\tilde{\mathbf{H}} = -\frac{\hbar}{2} \begin{pmatrix} \delta - \zeta t & \bar{\Omega}_{eff}(t)e^{i\Delta\phi} \\ \bar{\Omega}_{eff}^*(t)e^{-i\Delta\phi} & -\delta + \zeta t \end{pmatrix}. \tag{36}$$

Note that we do not require completely overlapped pulses here.

3.3 Nonimpulsive Case

In some excitation schemes, because of selection rules that take into consideration the polarization of the external field, the pump and Stokes field interact only with the corresponding transitions, and the general Hamiltonian can be simplified. For

that case, we can obtain the correct form of the Hamiltonian by putting $\bar{\Omega}_{p0}(t) = \bar{\Omega}_{s0}(t) = 0$ in Eqs. 25, 26, and 33. It results in

$$\Omega_{ac0}(t) = \frac{1}{2\Delta_p} \Omega_{p0}^2(t), \quad (37)$$

$$\Omega_{ac1}(t) = \frac{1}{2\Delta_p} \Omega_{s0}^2(t), \quad (38)$$

$$\Omega_{dif}(t) = \frac{1}{4\Delta_p} [\Omega_{p0}^2(t) - \Omega_{s0}^2(t)], \quad (39)$$

$$\bar{\Omega}_{eff}(t) = \frac{\Omega_{p0}(t)\Omega_{s0}(t)}{2\Delta_p}. \quad (40)$$

Therefore, in the field interaction representation, the Hamiltonian has the form

$$\tilde{\mathbf{H}} = -\frac{\hbar}{2} \begin{pmatrix} \delta(t) & \bar{\Omega}_{eff}(t)e^{i\Delta\phi} \\ \bar{\Omega}_{eff}^*(t)e^{-i\Delta\phi} & -\delta(t) \end{pmatrix}, \quad (41)$$

where

$$\delta(t) = \delta + (\alpha_s - \alpha_p)t + [\Omega_{p0}^2(t) - \Omega_{s0}^2(t)] / 4\Delta_p. \quad (42)$$

3.4 Adiabatic Solution

The Hamiltonian in Eq. 41 controls the dynamics of the qubit wave function in the approximation of the adiabatic elimination of the trion state. Here we consider the adiabatic excitation of the qubit and find the adiabatic solution of the Schrödinger equation with the Hamiltonian in Eq. 41.

Since the phase factor, $e^{i\Delta\phi}$, of the coupling term in Eq. 41 is time independent, it is convenient to use the following transformation $|\Phi(t)\rangle = \mathbf{A} |\Psi(t)\rangle$, where

$$\mathbf{A} = |0\rangle\langle 0| + e^{i\Delta\phi} |1\rangle\langle 1| = e^{i\Delta\phi/2} e^{-i\Delta\phi \sigma_z/2}, \quad (43)$$

so that the new wave function is governed by the Hamiltonian

$$\bar{\mathbf{H}} = \mathbf{A} \tilde{\mathbf{H}} \mathbf{A}^{-1} = -\frac{\hbar}{2} \begin{pmatrix} \delta(t) & \Omega_e(t) \\ \Omega_e(t) & -\delta(t) \end{pmatrix} = -\frac{\hbar}{2} (\delta(t) \sigma_z + \Omega_e(t) \sigma_x). \quad (44)$$

To solve the Schrödinger equation in the adiabatic representation, we apply another transformation, $|\bar{\Phi}(t)\rangle = \mathbf{R}(t) |\Phi(t)\rangle$, where

$$\mathbf{R}(t) = \begin{pmatrix} \cos \theta(t) & \sin \theta(t) \\ -\sin \theta(t) & \cos \theta(t) \end{pmatrix} = e^{i\theta(t)\sigma_y}, \quad (45)$$

and $\tan[2\theta(t)] = \Omega_e(t) / \delta(t)$. In the new basis the Hamiltonian, Eq. 44, takes the form

$$\mathbf{H}(t) = \mathbf{R}(t) \bar{\mathbf{H}}(t) \mathbf{R}^{-1}(t) = \begin{pmatrix} -\frac{\hbar}{2} \sqrt{\delta^2(t) + \Omega_e^2(t)} & 0 \\ 0 & \frac{\hbar}{2} \sqrt{\delta^2(t) + \Omega_e^2(t)} \end{pmatrix} = -\hbar \lambda(t) \boldsymbol{\sigma}_z / 2, \quad (46)$$

where $\lambda(t) = \sqrt{\delta^2(t) + \Omega_e^2(t)}$.

As we see, the Hamiltonian in Eq. 46 is diagonal in the adiabatic basis, and we can readily write down the solution. However, since the transformation $\mathbf{R}(t)$ is time dependent, an additional nonadiabatic coupling term is present in the general Schrödinger equation

$$i\hbar |\dot{\bar{\Phi}}(t)\rangle = -\frac{1}{2} \hbar \lambda(t) \boldsymbol{\sigma}_z |\bar{\Phi}(t)\rangle - \hbar \dot{\theta}(t) \boldsymbol{\sigma}_y |\bar{\Phi}(t)\rangle, \quad (47)$$

where

$$\dot{\theta}(t) = -\frac{\Omega_e(t) \dot{\delta}(t) - \delta(t) \dot{\Omega}_e(t)}{2(\Omega_e^2(t) + \delta^2(t))}. \quad (48)$$

Neglecting the nonadiabatic coupling term in Eq. 47, we readily obtain for the qubit wave function in the original basis

$$|\Psi(t)\rangle = e^{i\frac{\Delta\phi}{2}\boldsymbol{\sigma}_z} e^{-i\theta(t)\boldsymbol{\sigma}_y} e^{i\frac{\Lambda(t)}{2}\boldsymbol{\sigma}_z} e^{i\theta(0)\boldsymbol{\sigma}_y} e^{-i\frac{\Delta\phi}{2}\boldsymbol{\sigma}_z} |\Psi(0)\rangle, \quad (49)$$

where $\Lambda(t) = \int_0^t dt' \lambda(t')$. The general form of the evolution operator in Eq. 49 is well justified if the following condition $|\Omega_e(t) \dot{\delta}(t) - \dot{\Omega}_e(t) \delta(t)| \ll \lambda^3(t)$ is valid.

In the case of completely overlapped pulses, $\Omega_{p0}(t) = \Omega_{s0}(t)$, with identical chirp rates, $\alpha_p = \alpha_s$, for the resonant qubit, $\delta(t) = \delta = 0$, we have $\theta(t) = \theta(0) = \pi/4$, and the transformation matrix becomes $\mathbf{R}(t) = \mathbf{R}(0) = e^{i\pi\boldsymbol{\sigma}_y/4}$. Therefore, the unitary evolution operator for the wave function of the resonant qubit takes the form

$$\begin{aligned} \mathbf{U}(t) &= \begin{pmatrix} \cos(S(t)/2) & ie^{i\Delta\phi} \sin(S(t)/2) \\ ie^{-i\Delta\phi} \sin(S(t)/2) & \cos(S(t)/2) \end{pmatrix} \\ &= \cos(S(t)/2) \mathbf{I} + i \sin(S(t)/2) (e^{i\Delta\phi} \boldsymbol{\sigma}_+ + e^{-i\Delta\phi} \boldsymbol{\sigma}_-) \\ &= \cos(S(t)/2) \mathbf{I} - i \sin(S(t)/2) (\mathbf{n} \cdot \boldsymbol{\sigma}) = e^{-iS(t) \mathbf{n} \cdot \boldsymbol{\sigma} / 2}, \end{aligned} \quad (50)$$

where $S(t) = \int_0^t dt' \Omega_e(t')$ is the effective pulse area, $\mathbf{n} = (-\cos \Delta\phi, \sin \Delta\phi, 0)$, $\sigma_{\pm} = (\sigma_x \pm i\sigma_y)/2$ are the Pauli raising and lowering operators, and $\sigma_{x,y,z}$ are the Pauli operators. The nonadiabatic coupling term, Eq. 48, is zero for the resonant qubit, and the solution of the Schrödinger equation in the adiabatic approximation, Eq. 50, is the exact solution.

The density plots of the population and coherence ($|a_0(T)a_1^*(T)|$) at the final time (after the pulse excitation) as a function of the effective pulse area, $S(T)$, and the dimensionless frequency chirp parameter, α' / τ_0^2 , described by the unitary evolution operator in Eq. 50 is depicted in Fig. 18. We use the Gaussian shape for the pulse envelopes, assuming that linear chirp is obtained by applying a linear optics technique, meaning that a transform-limited pulse of duration τ_0 is chirped, conserving the energy of the pulse. The temporal (α) and spectral (α') chirps are related as $\alpha = \alpha' \tau_0^{-4} / (1 + \alpha'^2 / \tau_0^4)$, where τ_0 is the transform-limited pulse duration. We observe the Rabi oscillation regime, when the population of the qubit states is changing between 0 and 1 while the coherence is changing between 0 and 1/2. This behavior does not depend on the chirp rate, since the effective Rabi frequency $\Omega_e(t)$ is determined by the product of the pump and Stokes Rabi frequencies: $\Omega_{p0,s0}(t) = \Omega_0 \exp\{-t^2 / (2\tau^2)\} / [1 + \alpha'^2 / \tau_0^4]^{1/4}$ with the chirp-dependent pulse duration $\tau = \tau_0 [1 + \alpha'^2 / \tau_0^4]^{1/2}$ and the amplitude.^{22,23}

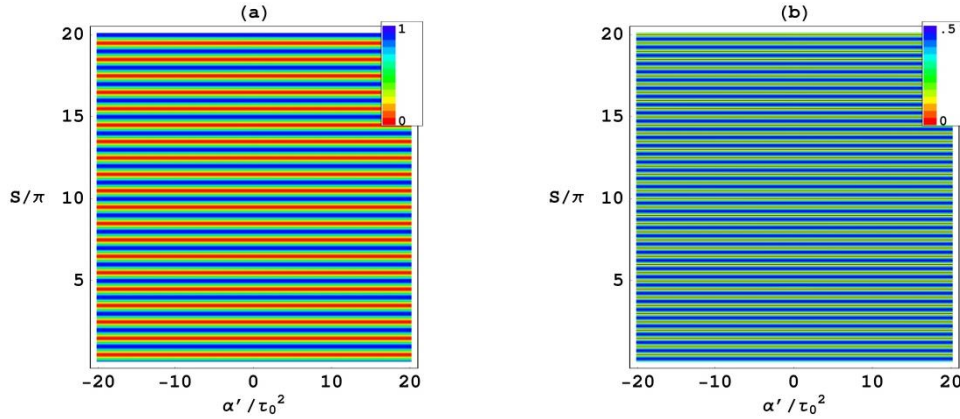


Fig. 18 The density plot of the $|1\rangle$ state population (a) and coherence (b) as a function of the effective pulse area and frequency chirp; $\alpha_p = \alpha_s$, $\delta = 0$. Initially, only the $|1\rangle$ state is populated.

In turn, for the off-resonant qubits, $\delta \neq 0$, the evolution operator in the adiabatic approximation takes the form

$$\mathbf{U}(t) = \begin{pmatrix} e^{i\xi(t)} \cos \theta(t) & -e^{-i\xi(t)} e^{i\Delta\phi} \sin \theta(t) \\ e^{i\xi(t)} e^{-i\Delta\phi} \sin \theta(t) & e^{-i\xi(t)} \cos \theta(t) \end{pmatrix}, \quad (51)$$

where

$$\cos \theta(t) = \frac{1}{\sqrt{2}} \sqrt{1 + \frac{\delta}{\sqrt{\delta^2 + \Omega_e^2(t)}}}, \sin \theta(t) = \frac{1}{\sqrt{2}} \sqrt{1 - \frac{\delta}{\sqrt{\delta^2 + \Omega_e^2(t)}}} \quad (52)$$

and $\xi(t) = \frac{1}{2} \int_0^t \sqrt{\delta^2 + \Omega_e^2(t')} dt'$ is the effective pulse area.

For the off-resonant case, the transformation matrixes are

$$\mathbf{R}^{-1}(t) = \begin{pmatrix} \cos \theta(t) & -\sin \theta(t) \\ \sin \theta(t) & \cos \theta(t) \end{pmatrix}, \quad R(0) = \begin{pmatrix} 1 & 0 \\ 0 & 1 \end{pmatrix}. \quad (53)$$

Figure 19 demonstrates excitation of the off-resonant qubit. As expected, the population of the off-resonant qubit at the final time is not changed by the external fields as long as the pulse excitation parameters are in the adiabatic regime. This is the regime of adiabatic return. However, we still observe the Rabi oscillation for the value of the chirp $|\alpha'| \lesssim 5\tau_0^2$. This is the area of nonadiabatic population transfer where the nonadiabatic coupling term cannot be neglected in Eq. 47.

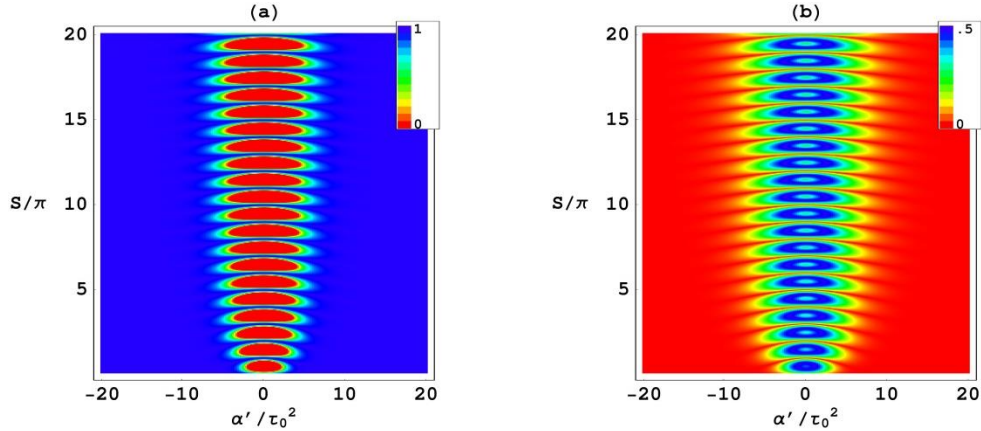


Fig. 19 The density plot of the $|1\rangle$ state population (a) and coherence (b) as a function of the effective pulse area and frequency chirp; $\alpha_p = \alpha_s$, $\delta\tau_0 = 0.75$. Initially, only the $|1\rangle$ state is populated.

3.5 Bloch Vector Representation

The dynamics of the qubit wave function can be described equally well using the Bloch vector representation. In addition, the Bloch vector formalism allows a very nice and clear geometrical interpretation of qubit dynamics.²⁴ In this section, we give a short overview of the Bloch picture.

A general state of a qubit can be described as

$$|\Psi\rangle = a_0(t)|0\rangle + a_1(t)|1\rangle = \cos(\beta/2)|0\rangle + e^{i\alpha} \sin(\beta/2)|1\rangle, \quad (54)$$

where α and β are the phase parameters. Up to an insignificant global phase, the wave function can be mapped into a unitary Bloch vector $\mathbf{B} = (u, v, w)$, as shown in Fig. 20.

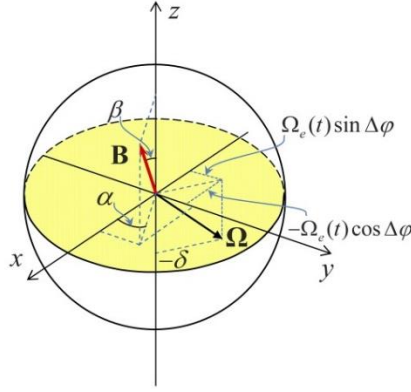


Fig. 20 The Bloch vector representation of the qubit state. Excitation of the qubit by an external field corresponds to the rotation of the \mathbf{B} vector about the pseudo field vector, Ω , with components determined by the effective Rabi frequency $\Omega_e(t)$, detuning δ , and the relative phase $\Delta\phi$.

To use Bloch vector representation, we construct the qubit density matrix

$$\rho = |\Psi\rangle\langle\Psi| = \begin{pmatrix} \varrho_{00} & \varrho_{01} \\ \varrho_{10} & \varrho_{11} \end{pmatrix} = \frac{1}{2} \begin{pmatrix} 1 + \cos \beta & e^{-i\alpha} \sin \beta \\ e^{i\alpha} \sin \beta & 1 - \cos \beta \end{pmatrix}, \quad (55)$$

where $\varrho_{ij} = a_i(t)a_j^*(t)$, $i, j = 0, 1$. Using a Pauli matrix decomposition

$$\begin{aligned} \rho &= \frac{1}{2} (\mathbf{I} + \mathbf{B} \cdot \vec{\sigma}) = \frac{1}{2} (\mathbf{I} + u \cdot \sigma_x + v \cdot \sigma_y + w \cdot \sigma_z) \\ &= \frac{1}{2} (\mathbf{I} + \cos \alpha \sin \beta \cdot \sigma_x + \sin \alpha \sin \beta \cdot \sigma_y + \cos \beta \cdot \sigma_z), \end{aligned} \quad (56)$$

we identify relation between the components of the qubit wave function, the qubit density matrix elements, and the Bloch vector components. Therefore, we obtain the following expression:

$$\mathbf{B} = \begin{pmatrix} u \\ v \\ w \end{pmatrix} = \begin{pmatrix} \varrho_{01} + \varrho_{10} \\ i(\varrho_{01} - \varrho_{10}) \\ \varrho_{00} - \varrho_{11} \end{pmatrix} = \begin{pmatrix} \cos \alpha \sin \beta \\ \sin \alpha \sin \beta \\ \cos \beta \end{pmatrix}. \quad (57)$$

Taking into account the Hamiltonian in Eq. 41, the equation of motion for the density matrix $i\hbar\dot{\boldsymbol{\rho}} = \mathbf{H}\boldsymbol{\rho} - \boldsymbol{\rho}\mathbf{H}$ takes the following explicit form

$$\begin{aligned} i\dot{\varrho}_{00} &= (e^{-i\Delta\phi}\varrho_{01} - e^{i\Delta\phi}\varrho_{10})\Omega_e(t)/2, \\ i\dot{\varrho}_{01} &= -\delta(t)\varrho_{01} - (\varrho_{11} - \varrho_{00})\Omega_e(t)e^{i\Delta\phi}/2, \\ i\dot{\varrho}_{10} &= \delta(t)\varrho_{10} + (\varrho_{11} - \varrho_{00})\Omega_e(t)e^{-i\Delta\phi}/2, \\ i\dot{\varrho}_{11} &= -(e^{-i\Delta\phi}\varrho_{01} - e^{i\Delta\phi}\varrho_{10})\Omega_e(t)/2. \end{aligned} \quad (58)$$

Using the relations in Eq. 57, we can also write the dynamic equation in the Bloch vector representation as

$$\begin{aligned} \dot{u} &= v\delta(t) + w\Omega_e(t)\sin\Delta\phi, \\ \dot{v} &= -u\delta(t) + w\Omega_e(t)\cos\Delta\phi, \\ \dot{w} &= -u\Omega_e(t)\sin\Delta\phi - v\Omega_e(t)\cos\Delta\phi. \end{aligned} \quad (59)$$

Introducing a pseudo field vector, $\boldsymbol{\Omega}$, with components determined by the effective Rabi frequency, 2-photon detuning, and the relative phase between pump and Stokes pulses,

$$\boldsymbol{\Omega} = \begin{pmatrix} -\Omega_e(t)\cos\Delta\phi \\ \Omega_e(t)\sin\Delta\phi \\ -\delta(t) \end{pmatrix}, \quad (60)$$

we can rewrite Eq. 59 in the compact form

$$\dot{\mathbf{B}} = \boldsymbol{\Omega} \times \mathbf{B}. \quad (61)$$

This is the Bloch equation, which describes a precession of the Bloch vector, \mathbf{B} , about the pseudo field vector, $\boldsymbol{\Omega}$, and allows clear, intuitive interpretation of qubit dynamics.

3.6 Evolution Operator of the Bloch Vector

Since we already know the exact form of the evolution operator $\mathbf{U}(t)$ in Eq. 50 and

$$|\Psi(t)\rangle = \mathbf{U}(t) |\Psi(0)\rangle, \quad (62)$$

we can easily construct the evolution operator for the Bloch vector. Using the definition of the density matrix, we have

$$\boldsymbol{\rho}(t) = |\Psi(t)\rangle\langle\Psi(t)| = \mathbf{U}(t) |\Psi(0)\rangle\langle\Psi(0)| \mathbf{U}^\dagger(t) = \mathbf{U}(t) \boldsymbol{\rho}(0) \mathbf{U}^\dagger(t), \quad (63)$$

where

$$\boldsymbol{\rho}(0) = |\Psi(0)\rangle\langle\Psi(0)| = \begin{pmatrix} \varrho_{00}(0) & \varrho_{01}(0) \\ \varrho_{10}(0) & \varrho_{11}(0) \end{pmatrix} = \frac{1}{2} \begin{pmatrix} 1+w_0 & u_0 - iv_0 \\ u_0 + iv_0 & 1-w_0 \end{pmatrix}$$

is the initial condition and

$$\begin{aligned} \mathbf{U}^\dagger(t) &= \begin{pmatrix} \cos(S(t)/2) & -ie^{i\Delta\phi} \sin(S(t)/2) \\ -ie^{-i\Delta\phi} \sin(S(t)/2) & \cos(S(t)/2) \end{pmatrix} \\ &= \cos(S(t)/2) \mathbf{I} - i \sin(S(t)/2) (e^{i\Delta\phi} \boldsymbol{\sigma}_+ + e^{-i\Delta\phi} \boldsymbol{\sigma}_-) \\ &= \cos(S(t)/2) \mathbf{I} + i \sin(S(t)/2) (\mathbf{n} \cdot \boldsymbol{\sigma}) = e^{iS(t)\mathbf{n} \cdot \boldsymbol{\sigma}/2}. \end{aligned} \quad (64)$$

Therefore,

$$\begin{aligned} \boldsymbol{\rho}(t) &= \mathbf{U}(t) \boldsymbol{\rho}(0) \mathbf{U}^\dagger(t) = \begin{pmatrix} \cos(S(t)/2) & ie^{i\Delta\phi} \sin(S(t)/2) \\ ie^{-i\Delta\phi} \sin(S(t)/2) & \cos(S(t)/2) \end{pmatrix} \\ &\quad \begin{pmatrix} \varrho_{00}(0) & \varrho_{01}(0) \\ \varrho_{10}(0) & \varrho_{11}(0) \end{pmatrix} \begin{pmatrix} \cos(S(t)/2) & -ie^{i\Delta\phi} \sin(S(t)/2) \\ -ie^{-i\Delta\phi} \sin(S(t)/2) & \cos(S(t)/2) \end{pmatrix}. \end{aligned} \quad (65)$$

Taking into account Eq. 57, we obtain for the Bloch vector:

$$\mathbf{B}(t) = \begin{pmatrix} C^2 + S^2 \cos(2\Delta\phi) & -S^2 \sin(2\Delta\phi) & 2C \cdot S \sin(\Delta\phi) \\ -S^2 \sin(2\Delta\phi) & C^2 - S^2 \cos(2\Delta\phi) & 2C \cdot S \cos(\Delta\phi) \\ -2C \cdot S \sin(\Delta\phi) & -2C \cdot S \cos(\Delta\phi) & C^2 - S^2 \end{pmatrix} \mathbf{B}(0), \quad (66)$$

where $C = \cos(S(t)/2)$, $S = \sin(S(t)/2)$.

3.7 Ultrafast Qubit Rotations Using Geometrical Phase

At this point, we are ready to discuss implementation of the single qubit gates since we have obtained the analytic solution for the qubit wave function and constructed the evolution operator in the Bloch vector representation. A universal

set of quantum gates has been intensively discussed in the literature related to the universality in quantum computation.²⁵ To perform quantum computation, we must have 2 major building blocks at our disposal: arbitrary unitary operations on a single qubit and a controlled-NOT operation on 2 qubits. Here we address only single qubit manipulation.

To demonstrate arbitrary geometric operations on a single qubit, we use the Bloch vector representation discussed in the previous section. Since any unitary rotation of the Bloch vector can be decomposed as

$$\mathbf{U} = e^{i\alpha_0} \mathbf{R}_z(\alpha_1) \mathbf{R}_y(\alpha_2) \mathbf{R}_z(\alpha_3), \quad (67)$$

where $\mathbf{R}_i = e^{i\alpha_i \sigma_i}$ ($i = y, z$) are the rotation operators, we need to demonstrate rotations of the qubit Bloch vector about the z and y axes by applying various sequences of external pulses. The decomposition in Eq. 67 plays an important role in circuit-based quantum computing, as it shows explicitly that 2 single-qubit operations allow us to create the arbitrary state of the qubit. Here we show how this can be accomplished by controlling the parameters of the external pulses, which are defined by the explicit form of the evolution operator (see Eq. 50). There are 2 distinct ways of the implementation of rotation, depending on which part of the total qubit phase we employ: dynamical or geometrical. Quantum gates relying on geometrical quantum phases are called holonomic gates, and they are expected to be robust with respect to noise.^{16,17}

To implement the rotation of the Bloch vector about the z axis (the phase gate) based on the geometrical phase, we can use the evolution operator of the resonant qubit, Eq. 50. The product of 2 evolution operators corresponding to the sequence of 2π pulses with the relative phase $\Delta\phi = \varphi + \pi$ gives

$$\mathbf{R}_z(\varphi) = \mathbf{U}_{\pi; \varphi + \pi} \mathbf{U}_{\pi; 0} = \begin{pmatrix} e^{i\varphi} & 0 \\ 0 & e^{-i\varphi} \end{pmatrix}, \quad (68)$$

where the first subindex of \mathbf{U} indicates the pulse area, $S(T)$, and the second one indicates the phase, $\Delta\phi$.

Figure 21 shows the Bloch vector trajectories of the qubit basis states $|0\rangle$ and $|1\rangle$, which correspond to the angles $\beta = 0$ and $\beta = \pi$ in Eq. 57 and the Bloch vector initially pointing in z and $-z$ directions while the vector $\mathbf{\Omega}_1 = (-\Omega_e, 0, 0)$ is pointing in $-x$ direction. For simplicity, we chose $\Delta\phi = 0$ for the first π -pulse. The first π -pulse flips the population to the state $|1\rangle$ ($|0\rangle$); correspondingly, the Bloch vector turns about the effective field vector $\mathbf{\Omega}_1$ (about the x axis), and it stays in the y, z plane all the time and points in the $-z$ (z) direction at the end of

the pulse. Because of the second π -pulse, the population is transferred back to the initial state $|0\rangle$ ($|1\rangle$); therefore, the Bloch vector returns to its original position pointing along the z ($-z$) axis. However, since we chose $\Delta\phi = \varphi + \pi$ for the second π -pulse, the pseudo-field vector is rotated counterclockwise by the angle $\varphi + \pi$ in the x, y plane, $\mathbf{\Omega}_2 = (\Omega_e \cos \varphi, -\Omega_e \sin \varphi, 0)$, and the Bloch vector moves in the plane perpendicular to the x, y plane and has the angle $\pi/2 - \alpha$ ($-\pi/2 - \alpha$) with the x, z plane.

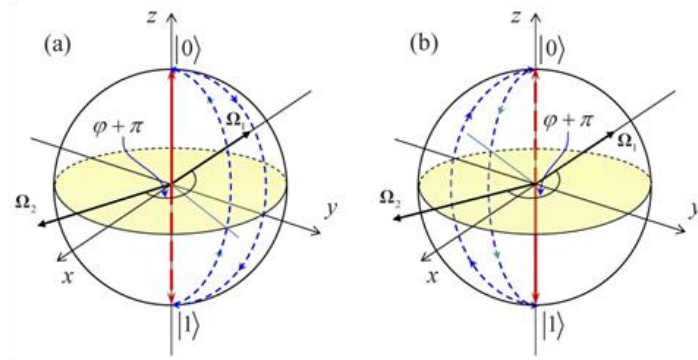


Fig. 21 The Bloch vector trajectory for the qubit state $|0\rangle$ in panel (a) and the qubit state $|1\rangle$ in panel (b) generated by the sequence of 2 π -pulses with the relative phase $\varphi + \pi$

The Bloch vectors representing a pair of orthogonal basis states $|0\rangle$ and $|1\rangle$ follow a path enclosing correspondingly solid angles of 2φ and -2φ . The geometrical phase is equal to one-half of the solid angle, which means the basis states $|0\rangle$ and $|1\rangle$ gain phases φ and $-\varphi$, and the evolution operator takes the form of the phase gate, Eq. 68, with the relative phase controlling the phase of the gate.

The rotation operator about the y axis can be constructed using 3 pulses. The first and third pulse is $\pi/2$ -pulse with $\Delta\phi = 0$, while the second pulse is π -pulse with the relative phase $\pi + \varphi$. It is easy to show, using Eq. 50, that this 3-pulse sequence results in

$$\mathbf{R}_y(\varphi) = \mathbf{U}_{\frac{\pi}{2};0} \mathbf{U}_{\pi;\pi+\varphi} \mathbf{U}_{\frac{\pi}{2};0} = e^{i\varphi \sigma_y}. \quad (69)$$

To demonstrate the geometrical nature of the $\mathbf{R}_y(\varphi)$ operation, we use the fact that it creates the relative phase between the qubit basis states $|\pm i\rangle = (|0\rangle \pm i|1\rangle) / \sqrt{2}$. In the Bloch representation, these states have the form

$$|\pm i\rangle = \cos\left(\frac{\pi}{4}\right)|0\rangle + e^{\pm i\frac{\pi}{2}} \sin\left(\frac{\pi}{4}\right)|1\rangle,$$

which are 2 vectors defined by the angles $\beta = \pi/2$ and $\alpha = \pm\pi/2$ and pointing in the y and $-y$ directions, as shown in Fig. 22. The trajectory of the Bloch vector representing the states $|\pm i\rangle$ is shown in Fig. 22. The pseudo-field vectors Ω_1 and Ω_3 are defined by the effective Rabi frequencies of the first and third pulses and are pointing in the $-x$ direction since $\Delta\phi = 0$. The second pseudo-field vector Ω_2 is rotated counterclockwise by the angle $\varphi + \pi$ in the x, y plane, the same as in the case above. The initial Bloch vector is pointing in the y ($-y$) direction. The first $\pi/2$ -pulse rotates the Bloch vector about Ω_1 to the position of the state $|1\rangle$ ($|0\rangle$). The second pulse flips the direction of the Bloch vector. The third $\pi/2$ -pulse returns the Bloch vector to its original position. The Bloch vector and the pseudo-field vector are orthogonal during the whole evolution. Similar to the previous case, we observe that the basis states $|i\rangle$ and $|-i\rangle$ follow a path enclosing correspondingly solid angles of 2φ and -2φ . Therefore, they gain the relative phase 2φ , which is the geometrical phase defined by the relative phase between pulses. It is easy to show that the phase gate in the $|\pm i\rangle$ basis is equivalent to the $\mathbf{R}_y(\varphi)$ gate in the $|0\rangle, |1\rangle$ basis.

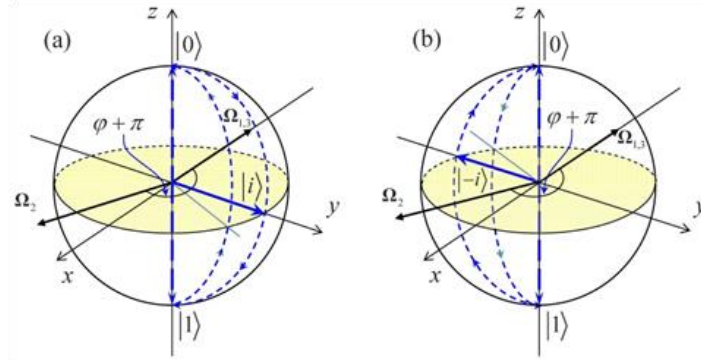


Fig. 22 The Bloch vector trajectory for the qubit state $|i\rangle$ in panel (a) and the qubit state $|-i\rangle$ in panel (b) generated by the sequence of 2 $\pi/2$ -pulses and one π pulse with the relative phase $\varphi + \pi$

3.8 Rotation in the Bloch Representation

Rotation operations in the Schrödinger picture are

$$|\Psi\rangle = \mathbf{R}_i |\Psi_0\rangle, \quad (70)$$

where $i = \{x, y, z\}$, $|\Psi_0\rangle$ is the initial wave function,

$$\mathbf{R}_x = e^{i\varphi \sigma_x} = \begin{pmatrix} \cos \varphi & i \sin \varphi \\ i \sin \varphi & \cos \varphi \end{pmatrix},$$

$$\mathbf{R}_y = e^{i\varphi \sigma_y} = \begin{pmatrix} \cos \varphi & \sin \varphi \\ -\sin \varphi & \cos \varphi \end{pmatrix},$$

$$\mathbf{R}_z = e^{i\varphi \sigma_z} = \begin{pmatrix} e^{i\varphi} & 0 \\ 0 & e^{-i\varphi} \end{pmatrix}.$$

Therefore, for the density matrix, we have

$$\boldsymbol{\rho} = |\Psi\rangle\langle\Psi| = \mathbf{R}_i |\Psi_0\rangle\langle\Psi_0| \mathbf{R}_i^{-1} = \mathbf{R}_i \boldsymbol{\rho}_0 \mathbf{R}_i^{-1}, \quad (71)$$

where $\boldsymbol{\rho}_0 = |\Psi_0\rangle\langle\Psi_0|$ is the initial density matrix.

Using equation

$$\mathbf{B} = Tr[\vec{\sigma} \boldsymbol{\rho}] = (Tr[\sigma_x \boldsymbol{\rho}], Tr[\sigma_y \boldsymbol{\rho}], Tr[\sigma_z \boldsymbol{\rho}]) = (u, v, w),$$

we find the following expressions for the transformation of the Bloch vector components

$$u = Tr[\sigma_x \mathbf{R}_i \boldsymbol{\rho}_0 \mathbf{R}_i^{-1}],$$

$$v = Tr[\sigma_y \mathbf{R}_i \boldsymbol{\rho}_0 \mathbf{R}_i^{-1}],$$

$$w = Tr[\sigma_z \mathbf{R}_i \boldsymbol{\rho}_0 \mathbf{R}_i^{-1}].$$

We obtain

$$\mathbf{R}_x = \begin{pmatrix} 1 & 0 & 0 \\ 0 & \cos(2\varphi) & \sin(2\varphi) \\ 0 & -\sin(2\varphi) & \cos(2\varphi) \end{pmatrix}, \quad (72)$$

$$\mathbf{R}_y = \begin{pmatrix} \cos(2\varphi) & 0 & -\sin(2\varphi) \\ 0 & 1 & 0 \\ \sin(2\varphi) & 0 & \cos(2\varphi) \end{pmatrix}, \quad (73)$$

$$\mathbf{R}_z = \begin{pmatrix} \cos(2\varphi) & \sin(2\varphi) & 0 \\ -\sin(2\varphi) & \cos(2\varphi) & 0 \\ 0 & 0 & 1 \end{pmatrix}. \quad (74)$$

The evolution operator in the Bloch representation is

$$\mathbf{U}(t) = \begin{pmatrix} C^2 + S^2 \cos(2\Delta\phi) & -S^2 \sin(2\Delta\phi) & 2C \cdot S \sin(\Delta\phi) \\ -S^2 \sin(2\Delta\phi) & C^2 - S^2 \cos(2\Delta\phi) & 2C \cdot S \cos(\Delta\phi) \\ -2C \cdot S \sin(\Delta\phi) & -2C \cdot S \cos(\Delta\phi) & C^2 - S^2 \end{pmatrix}. \quad (75)$$

Therefore, to demonstrate, for example, the \mathbf{R}_z rotation in the Bloch picture, we see that the first π pulse with the relative phase $\Delta\phi=0$ gives for the evolution operator

$$\mathbf{U}_{\pi;0} = \begin{pmatrix} 1 & 0 & 0 \\ 0 & -1 & 0 \\ 0 & 0 & -1 \end{pmatrix}. \quad (76)$$

The second π pulse with the relative phase $\Delta\phi=\pi+\varphi$ gives for the evolution operator

$$\mathbf{U}_{\pi;\pi+\varphi} = \begin{pmatrix} \cos(2(\pi+\varphi)) & -\sin(2(\pi+\varphi)) & 0 \\ -\sin(2(\pi+\varphi)) & -\cos(2(\pi+\varphi)) & 0 \\ 0 & 0 & -1 \end{pmatrix}. \quad (77)$$

Finally, the sequence of $\mathbf{U}_{\pi;\pi+\varphi}$ and $\mathbf{U}_{\pi;0}$ results in

$$\begin{aligned} \mathbf{U}_{\pi;\pi+\varphi} \mathbf{U}_{\pi;0} &= \begin{pmatrix} \cos(2(\pi+\varphi)) & -\sin(2(\pi+\varphi)) & 0 \\ -\sin(2(\pi+\varphi)) & -\cos(2(\pi+\varphi)) & 0 \\ 0 & 0 & -1 \end{pmatrix} \begin{pmatrix} 1 & 0 & 0 \\ 0 & -1 & 0 \\ 0 & 0 & -1 \end{pmatrix} \\ &= \begin{pmatrix} \cos(2\varphi) & \sin(2\varphi) & 0 \\ -\sin(2\varphi) & \cos(2\varphi) & 0 \\ 0 & 0 & 1 \end{pmatrix}, \end{aligned} \quad (78)$$

Similarly, one could consider the \mathbf{R}_y rotation in the Bloch picture.

3.9 Generalization of the Single-Qubit Operation Using Bright-Dark Basis

In the previous sections, we have considered several excitation schemes of the 3-level system and discussed a possible implementation of single-qubit gates. It was shown that all possible qubit states can be created in a controllable fashion using a couple of completely overlapped laser pulses, $\Omega_p(t) = \Omega_s(t)$. In this section, we present a more general solution, which allows some additional flexibility in terms of the ratio of the pump and Stokes pulse amplitudes. Again, we address here the coherent Raman excitation in a 3-level Λ -type system consisting of the 2 lowest states of electron spin $|0\rangle \equiv |-X\rangle$ and $|1\rangle \equiv |X\rangle$ coupled through an intermediate trion state $|T\rangle$ (see Fig. 17) and assume that the trion state is far off-resonance with the external fields. In addition, we restrict our consideration to the

nonimpulsive regime and can then put $\bar{\Omega}_{P+}(t) = \bar{\Omega}_{S+}(t) = 0$ in Eq. 22 so that the Hamiltonian takes the form

$$\begin{aligned}
\mathbf{H} &= \mathbf{U}_{RWA}^{-1} \mathbf{H} \mathbf{U}_{RWA} - i\hbar \mathbf{U}_{RWA}^{-1} \dot{\mathbf{U}}_{RWA} \\
&= -\frac{\hbar}{2} \begin{pmatrix} 0 & 0 & \Omega_{P+} \\ 0 & -2\omega_B & \Omega_{S+} \\ \Omega_{P+}^* & \Omega_{S+}^* & -2\omega_T \end{pmatrix} + \hbar \begin{pmatrix} 0 & 0 & 0 \\ 0 & -\Delta\omega & 0 \\ 0 & 0 & -\omega_P \end{pmatrix} \\
&= -\frac{\hbar}{2} \begin{pmatrix} 0 & 0 & \Omega_{P+} \\ 0 & 2(\Delta\omega - \omega_B) & \Omega_{S+} \\ \Omega_{P+}^* & \Omega_{S+}^* & -2\Delta_P \end{pmatrix}, \tag{79}
\end{aligned}$$

where

$$\Delta_P = \omega_T - \omega_P,$$

$$\Delta\omega = \omega_P - \omega_S,$$

$$\Omega_{P+} = \Omega_{P0}(t)e^{i\phi_P(t)},$$

$$\Omega_{S+} = \Omega_{S0}(t)e^{i\phi_S(t)}, \text{ and}$$

$$\phi_{P,S}(t) = \phi_{P,S} + \alpha_{P,S}t^2/2.$$

Let us consider the case when $\Omega_{P0}(t) = \Omega_0(t) \cos \mathcal{G}$ and $\Omega_{S0}(t) = \Omega_0(t) \sin \mathcal{G}$ and keeping the same time-dependent envelope for the pump and Stokes Rabi frequencies while the mixing angle \mathcal{G} controls the ration between the maximum of the Rabi frequencies.

In the bright-dark basis, the Hamiltonian takes the form

$$\bar{\mathbf{H}} = \mathbf{R}_{bd} \mathbf{H} \mathbf{R}_{bd}^{-1} = \frac{\hbar}{2} \begin{pmatrix} 2\delta S^2 & 2\delta S C e^{-i\phi_+} & -\xi_+(t)\Omega_0(t) \\ 2\delta S C e^{i\phi_+} & 2\delta C^2 & e^{i\phi_+} \xi_-(t) S C \Omega_0(t) \\ -\xi_+^*(t)\Omega_0(t) & e^{-i\phi_+} \xi_-^*(t) S C \Omega_0(t) & 2\Delta_P \end{pmatrix}, \tag{80}$$

where

$$S = \sin \mathcal{G},$$

$$C = \cos \mathcal{G},$$

$$\phi_+ = \phi_P + \phi_S,$$

$$\xi_+(t) = e^{i\alpha t^2/2} C^2 + e^{i\beta t^2/2} S^2, \text{ and}$$

$$\xi_{-}(t) = e^{i\alpha t^2/2} - e^{i\beta t^2/2}.$$

In the resonant case, $\delta = 0$, we obtain

$$\bar{\mathbf{H}} = \mathbf{R}_{bd} \mathbf{H} \mathbf{R}_{bd}^{-1} = \frac{\hbar}{2} \begin{pmatrix} 0 & 0 & -\xi_{+}(t)\Omega_0(t) \\ 0 & 0 & e^{i\phi_{+}} \xi_{-}(t) SC \Omega_0(t) \\ -\xi_{+}^{*}(t)\Omega_0(t) & e^{-i\phi_{+}} \xi_{-}^{*}(t) SC \Omega_0(t) & 2\Delta_p \end{pmatrix}.$$

In the case of equal chirp rates, $\alpha = \beta$, we have

$$\bar{\mathbf{H}} = \mathbf{R}_{bd} \mathbf{H} \mathbf{R}_{bd}^{-1} = \frac{\hbar}{2} \begin{pmatrix} 2\delta S^2 & 2\delta SC e^{-i\phi_{+}} & -e^{i\alpha t^2/2} \Omega_0(t) \\ 2\delta SC e^{i\phi_{+}} & 2\delta C^2 & 0 \\ -e^{-i\alpha t^2/2} \Omega_0(t) & 0 & 2\Delta_p \end{pmatrix}.$$

In the 2-photon resonance case, $\delta = 0$, and equal chirp rates, $\alpha = \beta$, we have

$$\bar{\mathbf{H}} = \mathbf{R}_{bd} \mathbf{H} \mathbf{R}_{bd}^{-1} = \frac{\hbar}{2} \begin{pmatrix} 0 & 0 & -e^{i\alpha t^2/2} \Omega_0(t) \\ 0 & 0 & 0 \\ -e^{-i\alpha t^2/2} \Omega_0(t) & 0 & 2\Delta_p \end{pmatrix}.$$

We can see that $a_D(t) = a_D(0)$, and we are left with the system of 2 differential equations for the probability amplitudes $a_B(t)$ and $\tilde{b}(t)$. Making the adiabatic elimination of the excited state $|T\rangle$ (assuming that $\dot{\tilde{b}}(t) \approx 0$), we have

$$\tilde{b}(t) = \frac{1}{2\Delta_p} \Omega_0(t) e^{-i\alpha t^2/2} a_B(t),$$

and

$$i\dot{a}_B(t) = -\frac{1}{4\Delta_p} \Omega_0^2(t) a_B(t).$$

The solution is

$$a_B(t) = a_B(0) e^{-\frac{i}{4\Delta_p} \int_0^t \Omega_0^2(t') dt'}.$$

Therefore, the evolution operator for the 2-photon resonant excitation by the equally chirped pulses under condition of the adiabatic elimination of the trion state has the following form:

$$\begin{aligned}
\mathbf{U}(t) &= \mathbf{R}_{bd}^{-1} \begin{pmatrix} e^{\frac{i}{4\Delta_p} \int_0^t \Omega_0^2(t') dt'} & 0 & 0 \\ 0 & 1 & 0 \\ 0 & 0 & 1 \end{pmatrix} \mathbf{R}_{bd} \\
&= \begin{pmatrix} e^{i\phi_p} \cos \vartheta & -e^{-i\phi_s} \sin \vartheta & 0 \\ e^{i\phi_s} \sin \vartheta & e^{-i\phi_p} \cos \vartheta & 0 \\ 0 & 0 & 1 \end{pmatrix} \begin{pmatrix} e^{iS(t)} & 0 & 0 \\ 0 & 1 & 0 \\ 0 & 0 & 1 \end{pmatrix} \begin{pmatrix} e^{-i\phi_p} \cos \vartheta & e^{-i\phi_s} \sin \vartheta & 0 \\ -e^{i\phi_s} \sin \vartheta & e^{i\phi_p} \cos \vartheta & 0 \\ 0 & 0 & 1 \end{pmatrix} \\
&= \begin{pmatrix} e^{iS(t)} \cos^2 \vartheta + \sin^2 \vartheta & e^{i\Delta\phi} (e^{iS(t)} - 1) \sin \vartheta \cos \vartheta & 0 \\ e^{-i\Delta\phi} (e^{iS(t)} - 1) \sin \vartheta \cos \vartheta & \cos^2 \vartheta + e^{iS(t)} \sin^2 \vartheta & 0 \\ 0 & 0 & 1 \end{pmatrix}, \tag{81}
\end{aligned}$$

where $S(t) = \int_0^t \Omega_0^2(t') dt' / (4\Delta_p)$, and $\Delta\phi = \phi_p - \phi_s$.

For the qubit states, the evolution operator can be written as

$$\begin{aligned}
\mathbf{U}(t) &= e^{iS(t)/2} \begin{pmatrix} e^{iS(t)/2} \cos^2 \vartheta + e^{-iS(t)/2} \sin^2 \vartheta & e^{i\Delta\phi} (e^{iS(t)/2} - e^{-iS(t)/2}) \sin \vartheta \cos \vartheta \\ e^{-i\Delta\phi} (e^{iS(t)/2} - e^{-iS(t)/2}) \sin \vartheta \cos \vartheta & e^{-iS(t)/2} \cos^2 \vartheta + e^{iS(t)/2} \sin^2 \vartheta \end{pmatrix} \\
&= e^{iS(t)/2} \begin{pmatrix} \cos(S(t)/2) + i \sin(S(t)/2) \cos(2\vartheta) & ie^{i\Delta\phi} \sin(S(t)/2) \sin(2\vartheta) \\ ie^{-i\Delta\phi} \sin(S(t)/2) \sin(2\vartheta) & \cos(S(t)/2) - i \sin(S(t)/2) \cos(2\vartheta) \end{pmatrix} \\
&= e^{iS(t)/2} \left[\cos(S(t)/2) \mathbf{I} + i \sin(S(t)/2) (\cos(\Delta\phi) \sin(2\vartheta) \boldsymbol{\sigma}_x \right. \\
&\quad \left. - \sin(\Delta\phi) \sin(2\vartheta) \boldsymbol{\sigma}_y + \cos(2\vartheta) \boldsymbol{\sigma}_z) \right] \\
&= e^{iS(t)/2} e^{-iS(t) \mathbf{n} \cdot \boldsymbol{\sigma} / 2}, \tag{82}
\end{aligned}$$

where

$$\mathbf{n} = (-\cos(\Delta\phi) \sin(2\vartheta), \sin(\Delta\phi) \sin(2\vartheta), -\cos(2\vartheta)).$$

3.10 Electron Spin in a Quantum Dot as a Qubit

In the previous sections, we developed several methods of an arbitrary manipulation of a qubit wave function using the geometric phase. Now we apply the proposed scheme to electron spin states in a charged quantum dot. Because of quantum confinement, the state of the electron can be expressed as a product of the Bloch function and an envelope function, which has a typical scale of the quantum dot size, a few nanometers. The energy level structure and optical selection rules have been discussed in the literature.^{12–15} A commonly accepted energy level structure comprises 4 levels: the 2 electron spin states and 2 trion spin states. Figure 23 shows 2 arrangements of the energy levels and polarization selection rules, which provide a possibility of optical control for the electron spin qubit.

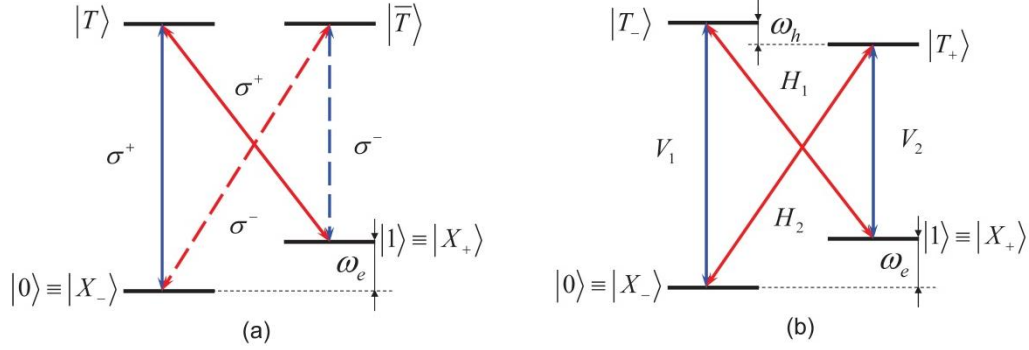


Fig. 23 Optical selection rules in different bases: (a) the mixed basis is used, where the electron spin states are in the x basis while the trion states are in the z basis; (b) coupling scheme is in the x basis.

The usual experiment of the electron spin control is performed at low temperature (~ 1 K). An external magnetic field in the Voigt configuration (of order $2 \div 7$ T) is applied along the x axis, perpendicular to the sample growth direction, the z axis. Zeeman splitting of the electron and trion spin states is on the order $\omega_e = 10$ meV and $\omega_h = 10 \mu\text{eV}$, correspondingly. At these conditions, taking into account the optical selection rules, the 4-level system can be considered as a double Λ -system. This coupling scheme is shown in Fig. 23b, where we indicated by H and V the optical field couplings with the orthogonal polarization. The shown coupling scheme is in the so-called x basis.

An alternative arrangement is depicted in Fig. 23a. In this case the mixed basis is used, where the electron spin states are in the x basis while the trion states are in the z basis. Using the 2 σ^+ or σ^- polarized fields, one can couple the electron spin states $|X_- \rangle$ and $|X_+ \rangle$, as shown in the Fig. 23a. This is the case where our 3-level model can be implemented. The corresponding Hamiltonian has the form obtained in Eq. 48. Assuming large detunings of the pump and Stokes field frequencies from the transition frequencies to the trion state $|T \rangle$, after the adiabatic elimination of the trion state, for the case of completely overlapped, identically linearly chirped pump and Stokes pulses, we obtain the following Hamiltonian

$$\mathbf{H} = -\frac{\hbar}{2} \begin{pmatrix} \delta & \Omega_e(t)e^{i\Delta\phi} \\ \Omega_e^*(t)e^{-i\Delta\phi} & -\delta \end{pmatrix}, \quad (83)$$

where $\delta = \omega_e - \Delta\omega$, and $\Delta\omega = \omega_p - \omega_s$, $\Omega_e(t) = \Omega_{p0}(t)\Omega_{s0}(t)[1 + e^{-i(\Delta\phi + \Delta\omega t)}]^2 / (2\Delta)$ is the effective 2-photon Rabi frequency, $\Delta = \omega_T - \omega_p$, and $\Delta\phi = \phi_p - \phi_s$. Note that here we have used $\mu_{0T} \approx \mu_{1T}$.

Now we show that the contribution of this oscillating term can be neglected when the pulse duration is longer than $\Delta\omega^{-1} \approx \omega_e^{-1}$. To demonstrate this and justify the procedure of the adiabatic elimination of the trion state, we numerically solve the time-dependent Schrödinger equation with the Hamiltonian in Eq. 48. That is, we compare our analytic solution with the exact solution of the Schrödinger equation without the adiabatic elimination approximation. An example of the comparison is shown in Fig. 24.

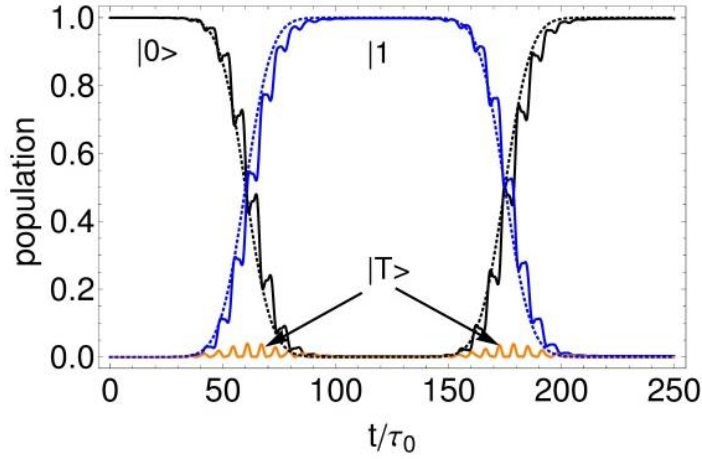


Fig. 24 The population dynamics of the resonant qubit states with (dotted lines) and without (solid lines) adiabatic elimination of the trion state in the 3-level system. The excitation is generated by the sequence of 2 pairs of π pulses (Gaussian pulse envelopes) with the relative phase $\Delta\phi = \pi/2$.

The example in Fig. 24 shows the dynamics of the population of the resonant qubit excited by a sequence of 2 pairs of linearly chirped pulses with the relative phase between the pairs being $\phi = \pi/2$. The parameters of the excitations are the transform-limited pulse duration $\tau_0 = 100$ fs, the pulse area of the pump and Stokes pulses is equal to π , linear chirp rate $\alpha' / \tau_0^2 = 20$, $\Delta\tau_0 = 6$, $\omega_e\tau_0 = 1$, the ratio between the maximum Rabi frequency and the single-photon detuning $\Omega_0 / \Delta = 0.77$. We observe a negligibly small amount of population in the trion state $|T\rangle$ at the intermediate time. The presented comparison also demonstrates a reasonable agreement between the proposed control schemes and the exact numerical solution. Note that the total time for the qubit operation in Fig. 24 is on the order of 25 ps, which is much shorter than the typical lifetime of the trion state as well as the time scale of other forms of decoherence, such as that induced by the electron-phonon interaction.

3.11 Possibility to Realize Geometric Gates Using Nitride Structures

We presented the analytic expression of the evolution operator of the electron spin in a quantum dot, which provides a clear geometrical interpretation of qubit dynamics. Using the analytic form of the evolution operator, we proposed a set of single-qubit rotations that are solely based on the geometrical phase. Our proposal combines the pulse area control with the adiabaticity by using chirped pulses. To estimate the time scale of the proposed operation, we can use the 100-fs pulses, which become picosecond pulses after linearly chirping. That amount of chirping is sufficient to provide adiabatic excitation²⁶ and can be readily produced experimentally using commercially available laser systems. Using parameters of the dipole moments $\mu_{0T,T1} \approx 200$ D available in InGaN/GaN,²⁷ GaN/AlN^{28,29} quantum dots, and detuning $\Delta = 5$ meV, we estimate the peak amplitude of the pulses on the order of $10^6 - 10^7$ V/m. The demonstrated adiabatic manipulation of a qubit using only the geometric phase has some advantages, since it reduces the requirements of perfect tuning of the control field parameters and is significantly more robust against noise.^{19,20}

4. Conclusions

We have shown that we can explain the kinetics of the photoexcited carriers in GaN and ZnO by including only carrier–carrier and carrier–phonon interactions and a relatively simple 2-band electronic structure model. Furthermore, we have presented a detailed analysis of the effect of different dephasing mechanisms on the carrier kinetics. Finally, we have experimentally measured and simulated using our theoretical model the temperature and pulse-power dependence of the photoluminescence spectra. We have found that carrier–carrier scattering is a principal dephasing mechanism in bulk GaN and ZnO for excitations below the LO phonon energy above the band edge. The coherent optical control of electronic excitations in these materials will require confined geometry, e.g., a quantum dot heterostructure, that will allow us to reduce the available density of final states in scattering processes. Our theoretical investigation shows the possibility to realize geometric quantum gates using nitride quantum dots.

5. References

1. Shishehchi S, Rudin S, Garrett GA, Wraback M, Bellotti E. J Appl Phys. 2013;114:233106.
2. Kuhn T, Rossi F. Phys Rev B. 1992;46:7496.
3. Haas S, Rossi F, Kuhn T. Phys Rev B. 1996;53:12855.
4. Haug H, Koch SW. Quantum theory of the optical and electronic properties of semiconductors. 3rd ed. World Scientific; 1994.
5. Jacoboni L, Lugli P. The Monte Carlo method for semiconductor device simulation. New York (NY): Springer-Verlag; 1989.
6. Osman MA, Ferry DK. Phys Rev B. 1987;36:6018.
7. Ridley BK. Quantum processes in semiconductors. 4th ed. Oxford (UK): Clarendon Press; 1999.
8. Shishehchi S, Garrett GA, Rudin S, Wraback M, Bellotti EJ. Electron Materials. 2014;43:3033.
9. Wang Y, Bellotti E, Wraback M, Rudin S. Proceedings of 27th Int. Conf. on the Physics of Semiconductors. Menendez J, Van de Walle CG, Editors. AIP 2005; 239.
10. Zebarjadi M, Bulutay C, Esfarjani K, Shakouri A. Appl Phys Lett. 2007;90:092111.
11. Lugli P, Ferry DK. IEEE Trans Electron Dev. 1985;ED-32:2431.
12. Press D, Ladd TD, Zhang B, Yamamoto Y. Nature. 2008;456:218–221.
13. Liu R-B, Yao W, Sham LJ. Adv Phys. 2010;59:703–802.
14. Chen P, Piermarocchi C, Sham LJ, Gammon D, Steel DG. Phys Rev A. 2004;69:075320.
15. Economou SE, Reinecke TL. Phys Rev Lett. 2007;99:217401.
16. Zanardi P, Rasetti M. Phys Lett A. 1999;264:94–99.
17. Jones JA, Vedral V, Ekert A, Castagnoli G. Nature. 2000;403:869–871.
18. Falci G, Fazio R, Palma GM, Siewert J, Vedral V. Nature. 2000;407:355–358.

19. De Chiara G, Palma GM. Phys Rev Lett. 2003;91:090404.
20. Lupo C, Aniello P. Phys Scr 2009;79:065012.
21. Bayer M, Ortner G, Stern O, Kuther A, Gorbunov AA, Forchel A, Hawrylak P, Fafard S, Hinzer K, Reinecke TL, Walck SN, Reithmaier JP, Klopff F, Schäfer F. Phys Rev B. 2002;65:195315.
22. Malinovsky VS, Krause JL. Phys. Rev. A. 2001;63:043415.
23. Malinovsky VS, Krause JL. Eur Phys J D. 2001;14:147–155.
24. Berman PR, Malinovsky VS. Principles of laser spectroscopy and quantum optics. Princeton (NJ): Princeton University Press; 2011.
25. Nielsen MA, Chuang IL. Quantum computation and quantum information. Cambridge (UK): Cambridge University Press, 2006.
26. Malinovskaya SA, Malinovsky VS. Opt Lett. 2007;32:707–709.
27. Ostapenko IA, Höning G, Kindel C, Rodt S, Strittmatter A. Appl Phys Lett. 2010;97:063103.
28. Andreev AD, O'Reilly EP. Appl Phys Lett. 2001;79:521–523.
29. Ranjan V, Allan G, Priester C, Delerue C. Phys Rev B 2003;68:115305.

6. Publications and Presentations for this DRI

- Garrett GA, Shishehchi S, Rudin S, Malinovsky V, Wraback M, Bellotti E. Experimental and theoretical study of dephasing processes in the kinetics of photoexcited carriers in GaN. *Phys Status Solidi C*. 2014;11(3–4):824–827. DOI 10.1002/pssc.201300688.
- Shishehchi S, Rudin S, Garrett GA, Wraback M, Bellotti E. Theoretical and experimental study of dynamics of photoexcited carriers in GaN. *J Appl Phys*. 2013;114:233106. <http://dx.doi.org/10.1063/1.4849856>.
- Shishehchi S, Garrett GA, Rudin S, Wraback M, Bellotti E. Theoretical and experimental study of time- and temperature-dependent photoluminescence in ZnO. *J Electron Materials*. 2014;43(8):3033–3040. DOI: 10.1007/s11664-014-3188-0.
- Malinovsky V, Rudin S. Ultrafast quantum gates for electron spin qubit in a quantum dot using geometric phase. *Proceedings of 7th International Conference on Quantum Dots*; 2012; Santa Fe, NM. p. 312.
- Malinovsky V, Rudin S. Geometric single-qubit gates for an electron spin in a quantum dot. *Int J Quantum Chemistry*. 2012;112(24):3744. DOI: 10.1002/qua.24202.
- Malinovsky V, Rudin S. Ultrafast control of electron spin in a quantum dot using geometric phase. *Solid State Electronics*. 2012;78:28–33. DOI: 10.1016/j.sse.2012.05.039.
- Malinovsky V, Rudin S. Adiabatic holonomic quantum gates for a single qubit. *Phys. Scripta*. 2014;T160:014029. <http://dx.doi.org/10.1088/0031-8949/2014/T160/014029>.
- Malinovsky V, Rudin S. Universal set of single-qubit gates based on geometric phase of electron spin in a quantum dot. 2012 APS March Meeting. Boston, MA. <http://www.aps.org/meetings/march/index.cfm>.
- Shishehchi S, Rudin S, Garrett G, Wraback M, Bellotti E. Theoretical and experimental study of kinetics of photoexcited carriers in wide band gap semiconductors. APS March Meeting 2013. Baltimore, MD. <http://www.aps.org/meetings/march/index.cfm>.
- Malinovsky V, Rudin S. Geometric single-qubit gates for an electron spin in a quantum dot. Sanibel Symposium; 2012 Feb 22; St. Simons Island, GA.

- Malinovsky V, Rudin S. Geometric Quantum Gates for an Electron-Spin Qubit in a Quantum Dot. 43rd Annual DAMOP Meeting/APS Abstract Book. 2012 Jun 4; Anaheim, CA.
- Shishehchi S, Rudin S, Garrett GA, Wraback M, Malinovsky V, Bellotti E. Theoretical and experimental study of dephasing processes in kinetics of photo-excited carriers in GaN. 10th International Conference on Nitride Semiconductors; 2013 Aug 25–30; Washington, DC.
- Malinovsky VS, Rudin S. Geometric quantum gates for electron spin qubit in a quantum dot. 20th Central European Workshop on Quantum Optics; 2013 Jun; Stockholm, Sweden.
- Garrett GA, Rudin S, Wraback M, Shishehchi S, Bellotti E. Temperature effects in the kinetics of photoexcited carriers in wide band gap semiconductors. 32th Int. Conf. on the Physics of Semiconductors; ICPS-32; 2014 Aug 10–14; Austin, TX.
- Malinovsky VS, Rudin S. Holonomic quantum gates for a single qubit. 54th Sanibel Symposium; 2014 May; University of FL.

1 DEFENSE TECHNICAL
(PDF) INFORMATION CTR
DTIC OCA

2 DIRECTOR
(PDF) US ARMY RESEARCH LAB
RDRL CIO LL
IMAL HRA MAIL & RECORDS
MGMT

1 GOVT PRINTG OFC
(PDF) A MALHOTRA

3 DIR USARL
(PDF) RDRL SEE I
G GARRETT
V MALINOVSKY
S RUDIN

INTENTIONALLY LEFT BLANK.